Doklady Physics, Vol. 50, No. 3, 2005, pp. 119–122. Translated from Doklady Akademii Nauk, Vol. 401, No. 2, 2005, pp. 181–84.

PHYSICS

Relaxation while Settling a Scaling-Invariant Distribution of Fluctuations in Random Processes with 1/*f* Noise

Corresponding Member of the RAS V. P. Koverda and V. N. Skokov

Received November 11, 2004

Among the numerous steady-state random processes, those in which the power spectrum is inversely proportional to the frequency *f*, i.e., the so-called "$\frac{1}{f}$" processes are of particular importance. They attract attention due to their scaling-invariant fluctuation distribution. In the general case, scaling invariance can be associated with the critical behavior or self-organization in complex systems [1]. An example of scaling-invariant behavior is the Kolmogorov turbulence when energy fluxes of various length scales arise in fluid flows, these phenomena obeying unified universal similarity laws [2]. However, not all random processes are reduced to such turbulence. Almost 80 years ago, electric-voltage fluctuations inversely proportional to the frequency were discovered in electronic devices (flicker-noise [3]). It turned out that random processes displayed by the $\frac{1}{f}$ spectrum may be encountered in a number of phenomena. In addition to the electric-current and magnetic fluctuations studied in solid-state physics, many random processes in astrophysics, geophysics, biology, and computer science also display a power spectrum inversely proportional to the frequency [4].

However, in spite of the wide prevalence of $\frac{1}{f}$ random processes in nature, a commonly used model for them is absent. Moreover, in various cases, different explanations are associated with the $\frac{1}{f}$ spectrum, and different models are constructed for its description. There have been numerous attempts to explain a possible generation mechanism for scaling-invariant fluctuations, which are based on the concept of self-organized criticality [5] applied to the description of complex systems with developed fluctuations.

Institute of Thermal Physics, Ural Division, Russian Academy of Sciences, ul. Amundsena 106, Yekaterinburg, 620016 Russia
e-mail: koverda@itp.uran.ru; vnskokov@itp.uran.ru

Studies of random processes occurring in the processes of the heat-and-mass transfer have shown that $\frac{1}{f}$ spectral fluctuations appear as a result of interactions between subcritical and supercritical nonequilibrium phase transitions in the presence of white noise [6]. In this case, the extended critical behavior of the fluctuations is characterized by a self-similar probability-density distribution independent of time. In this case, it is important to reveal the effect of initial conditions on the settling time of the steady-state fluctuation distribution function, to clarify a law determining (at arbitrary initial conditions) the relaxation of the random-process realization when a scaling-invariant distribution settles, and also to estimate the settling time. This is the basic topic of the present study.

In the theory of $\frac{1}{f}$ fluctuations of nonequilibrium phase transitions [7], stochastic equations are used for the description of fluctuation dynamics in a concentrated system. In the simplest case, these equations are of the form

$$\begin{aligned} \frac{d\phi}{dt} &= -\phi\psi^2 + \psi + \Gamma_1(t), \\ \frac{d\psi}{dt} &= -\phi^2\psi + 2\phi + \Gamma_2(t). \end{aligned} \tag{1}$$

Here, ϕ and ψ are dynamic variables (order parameters), whereas Γ_1 and Γ_2 correspond to the Gaussian δ-correlated noise. When this set of equations is written out in the form (1), Γ_1 and Γ_2 can have different realizations but identical dispersions. The multiplier 2 standing at the variable ϕ in the second equation of set (1) renders these equations nonequivalent and implies the existence of a certain uncompensated flux.

In order to integrate the set of Eqs. (1), we rewrite them in the form [8]

$$\begin{aligned} \phi_{i+1} &= (\phi_i + \psi_i\Delta t)(1 + \psi_i^2\Delta t)^{-1} + \xi_i\Delta t^{0.5}, \\ \psi_{i+1} &= (\psi_i + 2\phi_i\Delta t)(1 + \phi_i^2\Delta t)^{-1} + \eta_i\Delta t^{0.5}. \end{aligned} \tag{2}$$

1028-3358/05/5003-0119$26.00

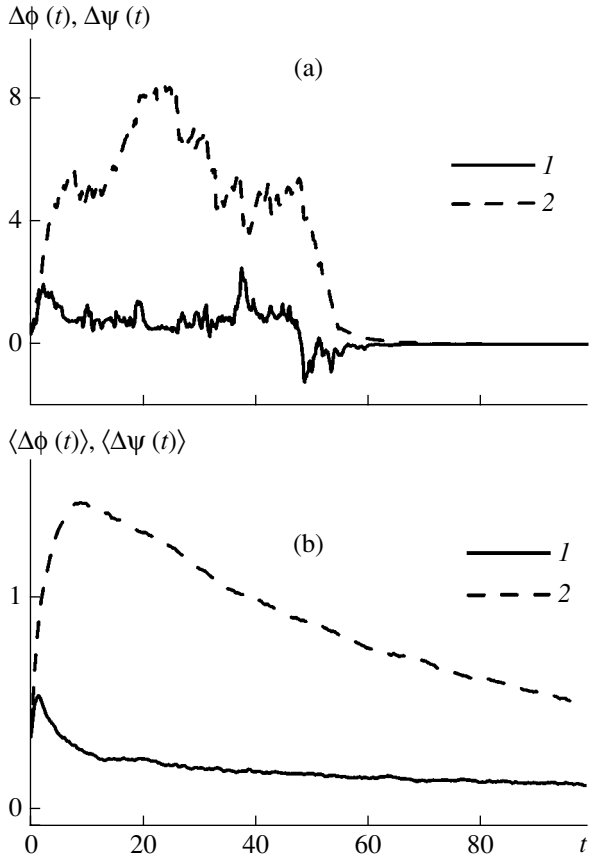

Fig. 1. Initial segments for the relaxation of system (2): (a) relaxations for separate realizations of random processes (*1*) $\Delta\phi(t)$ and (*2*) $\Delta\psi(t)$; (b) relaxations of random processes: (*1*) $\langle\Delta\phi(t)\rangle$ and (*2*) $\langle\Delta\psi(t)\rangle$ both averaged over the realization ensemble. The integration step is $\Delta t = 0.15$.

Here, ξ_i and η_i are the sequences of Gaussian random numbers with zero average value and with standard deviation σ, which model white noise. This form of equations is obtained when the values of ϕ_i and ψ_i in nonlinear terms of the first and second equations of set (1) are taken, respectively, not at the initial, but at the final point of the partition interval Δt_i. This ensures the stability of the numerical integration of set (1) under both arbitrary initial conditions and arbitrary integration steps Δt. It is worth noting that we can arrive at the same form of set (2) for the numerical integration in a more rigorous manner by summarizing (in the course of integrating the determinate part of the stochastic equations) the jumps within the time interval Δt_i not only for the first derivative, but for all successive derivatives of the functions $\phi(t)$ and $\psi(t)$. The corresponding Taylor series can be approximated by infinitely decreasing geometrical progressions. As a result, upon summarizing the jumps for all the derivatives, we obtain set (2). In order not to correct the values of standard deviations σ of Gaussian random numbers ξ_i and η_i with the variation of the integration step Δt, the differentials $\xi_i\Delta t^{0.5}$ and $\eta_i\Delta t^{0.5}$ in set (2) contain the time interval taken in the power of 0.5.

Set (1) and its calculation version (2) have a noise-induced transition with respect to the probability density $P(\sqrt{\phi^2\psi^2})$. The criticality vicinity for this transition determines the intensity of the external noise ($\sigma \simeq \sigma_c$) for which the system generates the stochastic processes $\phi(t)$ and $\psi(t)$. In these processes, the power spectra are inversely proportional to the frequency (i.e., $S_\phi \sim \frac{1}{f}$) and inversely proportional to the frequency squared ($S_\psi \sim \frac{1}{f^2}$), respectively [9]. However, the random function $\chi(t)$ inverse with respect to $\psi(t)$ has the spectrum inversely proportional to the first power of the frequency $S_\chi \sim \frac{1}{f}$, which coincides with the spectrum S_ϕ. In order to exclude large fluctuations of the function $\chi(t)$, the latter must be defined as the inverse function with respect to $\psi(t)$, for example,

$$\chi_i = \frac{\psi_i}{(\varepsilon + \psi_i^2)^{-1}}, \qquad (3)$$

where $\varepsilon \simeq 0.01$–0.02 is a small constant, and $\chi(t) = \frac{1}{\psi(t)}$ everywhere except in the vicinity of zeros of the function $\psi(t)$. In the vicinity of zeros, $\psi(t) = \chi(t)$ if $\psi \longrightarrow 0$. The function $\chi(t)$ is of interest because of the fact that it is scaling-invariant for virtually all time intervals [10].

Our goal is to study the relaxation process for the system described by set (1) while settling the scaling-invariant parameter distribution for different initial conditions. To do this, we consider the behavior of the differences $\Delta\phi = \tilde{\phi}(t) - \phi^0(t)$ and $\Delta\psi = \tilde{\psi}(t) - \psi^0(t)$ corresponding to different initial conditions. The numerical integration of set (2) has made it possible to analyze various initial conditions. It was found that in a case in which the same sequences of Gaussian random numbers $\{\xi_i\}$ and $\{\eta_i\}$ had been given, the random processes $\tilde{\phi}(t)$ and $\tilde{\psi}(t)$ independently of initial conditions converged to the same random functions $\phi(t)$ and $\psi(t)$ after a lapse of a certain time τ, i.e., $\Delta\phi(t) \longrightarrow 0$, $\Delta\psi(t) \longrightarrow 0$, as $t \gg \tau$. However, for certain realizations of the random process, this transition occurs in the form of a jump (Fig. 1a). In the case of averaging the relaxation over a large number of realizations, we can obtain a smooth relaxation dependence of $\langle\Delta\phi(t)\rangle$ and $\langle\Delta\psi(t)\rangle$, where skew brackets denote the time dependence averaged over the realizations. The typical averaged functions $\langle\Delta\phi(t)\rangle$ and $\langle\Delta\psi(t)\rangle$ are shown in Fig. 1b. In this case, the following calculated values of the parameters of set (2), namely, $\sigma = 0.85$, $\Delta t = 0.15$, and the step number $N = 400$ were used. The initial conditions were

$\phi^0(0) = \psi^0(0) = 0$ and $\tilde{\phi}(0) = \tilde{\psi}(0) = 0.3$. The curves in Fig. 1b are obtained by averaging over 500 random realizations of the process. In general, in calculations of the relaxation, the integration steps from 0.06 to 0.3 were used for the number of integration steps up to 16000 and for averaging up to 1000 realizations. Initial segments of the realizations are shown in Fig. 1.

We can now discuss general relaxation features while settling the scaling-invariant distribution of fluctuations in random processes featured by the $\frac{1}{f}$ spectrum.

Firstly, after a certain transition time t_0 (see Fig. 1b), the system under consideration becomes self-organized, and for $t > t_0$, the averaged relaxations $\langle\Delta\phi(t)\rangle$ and $\langle\Delta\psi(t)\rangle$ begin to obey the simple exponential form $\langle\Delta\phi(t)\rangle \sim \langle\Delta\psi(t)\rangle \sim \exp\left(-\frac{t}{\tau}\right)$, where τ is the characteristic time.

Secondly, while settling the scaling-invariant distribution in system (2), the characteristic relaxation time τ is inversely proportional to the integration step squared ($\tau \sim \Delta t^{-2}$) and remains the same for both processes $\langle\Delta\phi(t)\rangle$ and $\langle\Delta\psi(t)\rangle$. In Fig. 2, the relaxations $\langle\Delta\phi(t)\rangle$ and $\langle\Delta\psi(t)\rangle$ are plotted in semi-logarithmic coordinates. The estimation of the relaxation time yields $\tau \simeq 2\Delta t^{-2}$ for the integration steps employed.

Thirdly and finally, the transition time at the beginning of the relaxation is determined by the initial conditions and, in terms of order of magnitude, coincides with the relaxation time or is even shorter: $t_0 \le \tau$.

The general features of the relaxation while settling the scaling-invariant distribution are conserved not only for small differences in the initial conditions when this difference does not exceed the root-mean-square deviation corresponding to a settled steady-state random process but also for the case of large differences in initial conditions. However, it is worth noting that for large differences of initial conditions, the relaxation $\langle\Delta\phi(t)\rangle$ yields a new qualitative behavior during the transition period t_0, i.e., at the very beginning of the relaxation. If for small differences in the initial conditions the quantity $\langle\Delta\phi(t)\rangle$ can even slightly increase at the beginning of the relaxation (see Fig. 1b), then for large differences in the initial conditions (on the order of a standard deviation of a steady-state process or greater), $\langle\Delta\phi(t)\rangle$ at the initial period $t \le t_0$ obeys the power dependence of the relaxation: $\langle\Delta\phi(t)\rangle \sim t^{-0.5}$. In Fig. 3, this dependence is illustrated in the double-logarithmic scale. It should be noted that the relaxation of function $\langle\Delta\chi(t)\rangle$, where the function $\chi(t)$ is defined by formula (3), virtually entirely coincides with the relaxation behavior of the function $\langle\Delta\phi(t)\rangle$ (which is why the relaxation of function $\langle\Delta\chi(t)\rangle$ is not shown in the figures).

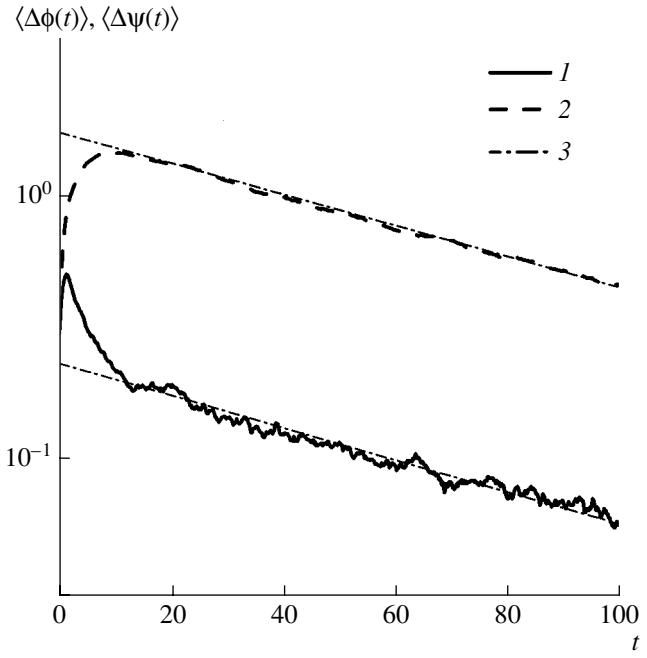

Fig. 2. Relaxations of random processes: (*1*) $\langle\Delta\phi(t)\rangle$; (*2*) $\langle\Delta\psi(t)\rangle$; and (*3*) dependence $\sim\exp\frac{t}{\tau}$ for $\tau \simeq 2\Delta t^{-2}$.

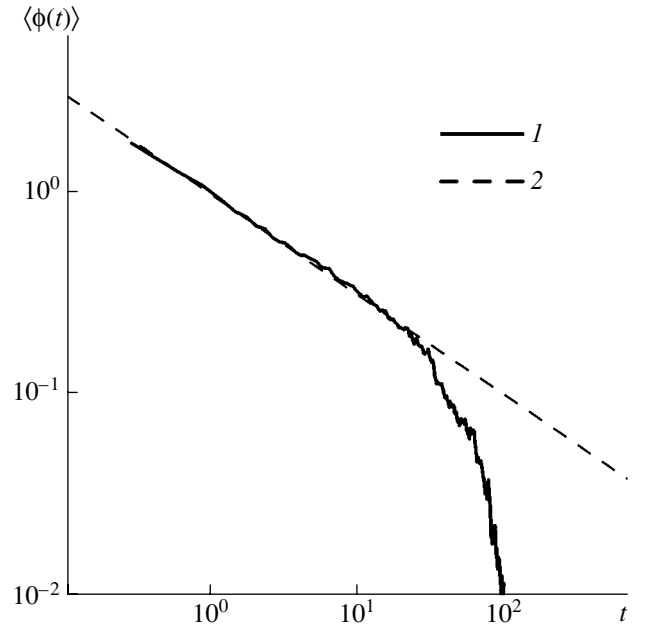

Fig. 3. Relaxation of a random process $\langle\Delta\phi(t)\rangle$: (*1*) for large differences in initial conditions and (*2*) the dependence $\sim t^{-0.5}$.

Thus, in this study, we have investigated the relaxation of fluctuation parameters for random processes with the $\frac{1}{f}$ spectrum as a function of initial conditions. In the given case, the relaxation of a steady-state random process is associated with settling the scaling-

invariant fluctuation distribution and obeys a simple exponential form. The characteristic settling time for the scaling-invariant fluctuation distribution is inversely proportional to integration step squared and coincides for all parameters of the model system that describes fluctuations with the $\frac{1}{f}$ spectrum.

ACKNOWLEDGMENTS

This work was supported by the Russian Foundation for Basic Research, project no. 03-02 16215.

REFERENCES

1. H. J. Jensen, *Self-Organized Criticality* (Cambridge Univ. Press, Cambridge, 1998).
2. A. N. Kolmogorov, Dokl. Akad. Nauk SSSR **30**, 299 (1941).
3. Sh. M. Kogan, Usp. Fiz. Nauk **145** (2), 285 (1985) [Sov. Phys. Usp. **28**, 170 (1985)].
4. Yu. L. Klimontovich, *Statistical Theory of Open Systems* (Yanus, Moscow, 1995; Kluwer, Dordrecht, 1995).
5. P. Bak, C. Tang, and K. Wiesenfeld, Phys. Rev. A **38**, 364 (1988).
6. V. N. Skokov, A. V. Koverda, A. V. Reshetnikov, *et al.*, Int. J. Heat Mass Transfer **46**, 1879 (2003).
7. V. P. Koverda, V. N. Skokov, and V. P. Skripov, Zh. Éksp. Teor. Fiz. **113** (5), 1748 (1998) [JETP **86**, 953 (1998)].
8. V. P. Koverda and V. N. Skokov, Dokl. Akad. Nauk **366** (2), 316 (1999) [Dokl. Phys. **44**, 350 (1999)].
9. V. P. Koverda and V. N. Skokov, Dokl. Akad. Nauk **386**, 187 (2002) [Dokl. Phys. **47**, 654 (2002)].
10. V. P. Koverda and V. N. Skokov, Dokl. Akad. Nauk **393**, 184 (2003) [Dokl. Phys. **48**, 615 (2003)].

Translated by G. Merzon

Doklady Physics, Vol. 50, No. 3, 2005, pp. 123–127. Translated from Doklady Akademii Nauk, Vol. 401, No. 3, 2005, pp. 324–328.

PHYSICS

Prismatic Carbon Nanotubes: Characteristic Features of Their Crystal Structure in Electron Diffraction Patterns and the Determination of Chirality Angle

L. D. Grigor'eva

Presented by Academician Yu.A. Osip'yan December 26, 2003

Received October 8, 2004

A multiwall carbon nanotube is a set of single-wall nanotubes embedded into each other, where the distance between tubes is equal to about 3.35 Å. The multiwall carbon nanotube is not always formed by coaxial cylinders. Increase in the tube diameter and in the number of walls causes deviations from cylindrical shape. In this case, faceted nanotubes formed by coaxial prisms embedded into each other can arise [1]. The structural features of prismatic tubes manifest themselves in electron diffraction patterns. The aim of this paper is to describe the characteristic features of electron diffraction patterns for prismatic carbon nanotubes and to determine the chirality angle for a faceted tube.

The arrangement of the reciprocal lattice for a tube is partially similar to that for a textured polycrystal: in both cases, the reciprocal lattice could be constructed based on that for the single crystal by rotation about a certain axis. For the textured polycrystal, the rotation of small single crystals forming the polycrystal occurs about such an axis. This gives rise to ring- or arc-shaped reflections that characterize the texture and belong to one band. Such a pattern occurs in the case of usual orientation of the texture when the electron beam is perpendicular to the sample plane and the basal plane of the texture. The latter is the plane of the preferred orientation (with respect to the external reference system) for microscopic single crystals forming the polycrystal.

For the carbon nanotube, the reciprocal lattice is formed by the rotation of the reciprocal lattice of the graphite *ab* plane about an axis arbitrarily oriented in this plane. In contrast to the texture, the tube axis at its usual orientation is parallel rather than perpendicular to the sample plane and, hence, it is perpendicular to the electron beam. As a result, the electron diffraction pattern for the tube is that cross-section of the reciprocal lattice which passes through the tube axis.

The upper panel of Fig. 1 shows the mutual orientation of axes for the direct and reciprocal lattices (*a*, *b*, *c* and *a**, *b**, *c** axes, respectively). This figure also demonstrates the main rows of lattice sites in the reciprocal lattice of graphite (10*l*, 11*l*, and 01*l*). If the electron beam is directed parallel to the *c* axis, the cross-section of the site rows by a plane corresponding to the diffraction sphere involves the lattice sites in the *a***b** plane. In the corresponding electron diffraction pattern, we should see the reflections arranged in the form of a

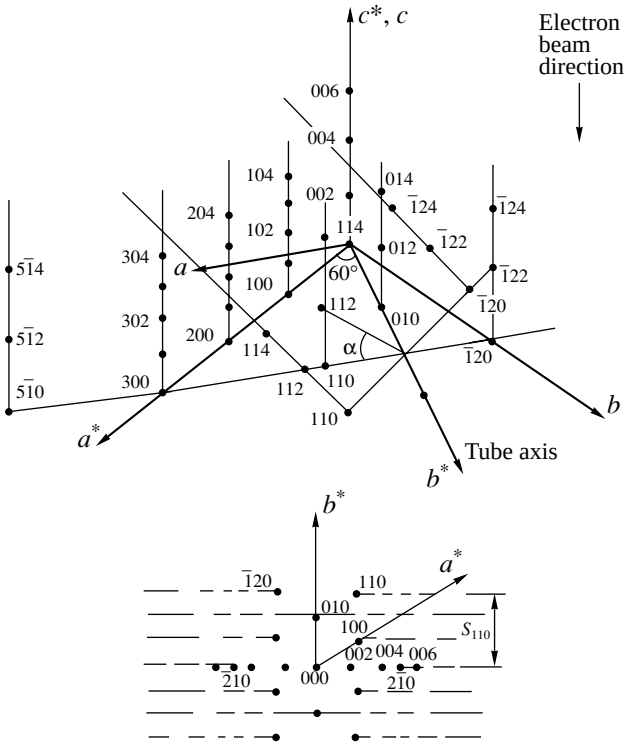

Fig. 1. Site rows in the graphite lattice. Upper panel: the reciprocal lattice of graphite. The rotation for site row 11*l* about the *b** axis by an angle of $\alpha = 36.2°$ is shown. Lower panel: the schematic electron diffraction pattern for the tube with zero chirality. The rays along which the displacement of reflections due to the lattice rotation occurs are shown.

Institute of Solid State Physics, Russian Academy of Sciences, Chernogolovka, Moscow oblast, 142432 Russia
e-mail: ldg@issp.ac.ru

1028-3358/05/5003-0123$26.00

characteristic hexagonal network. Using this graphite, let us make a tube in the form of a straight cylinder. To this end, we choose the direction of the tube axis in the *ab* plane and rotate the depicted reciprocal lattice about this axis. If the tube axis is parallel to the [120] direction, it corresponds to the [010]* direction, i.e. to the *b** axis in the reciprocal lattice. In this case, we have a zero chirality angle for the tube. Let us now rotate site rows $11l$, $30l$, $5\bar{1}l$, and $7\bar{2}l$, which are based on the line perpendicular to the *b** axis, about the *b** axis. If the rotation of the lattice is continuous, then the plane of the diffraction sphere will meet the lattice sites in the following sequence (when we start from site $7\bar{2}6$):

hkl	$7\bar{2}6$	$7\bar{2}4$	$7\bar{2}2$	$7\bar{2}0$	$5\bar{1}6$	$5\bar{1}4$	$5\bar{1}2$	$5\bar{1}0$	307	306
d_{hkl}, Å	0.3258	0.3337	0.3388	0.3406	0.4286	0.4473	0.4597	0.4641	0.5696	0.5984
hkl	305	304	303	302	301	300	116	114	112	110
d_{hkl}, Å	0.6266	0.6528	0.6757	0.6936	0.7050	0.7090	0.8259	0.9902	1.1529	1.2280

In this case, the electron diffraction pattern will contain a set of reflections lying in the ray that starts from the reflection (110) and is perpendicular to the rotation axis of the tube. Taking into account the rotation of the remaining site rows, we get the picture shown in the lower panel of Fig. 1. The distant reflections turn out to be located so close to each other that they merge into a single bar. Note that the efficient crossing with diffraction in the course of the rotation with the lattice, i.e., the crossing with a site in the site row, is possible only for some definite position of the row. For the aforementioned rows, the efficient crossings occur at the following tilting angles α (*hkl* is the reflection index appearing in the electron diffraction pattern as a result of the tilting of the site row):

hkl	110	300	$5\bar{1}0$	$7\bar{2}0$	$7\bar{2}2$	301	$5\bar{1}2$	$7\bar{2}4$	302	$5\bar{1}4$
α, deg	0.0000	0.0000	0.0000	0.0000	5.9713	6.9575	8.3310	11.8157	13.7156	16.3240
hkl	$7\bar{2}6$	303	$5\bar{1}6$	304	305	112	306	307	114	116
α, deg	17.4216	20.1073	23.7165	26.0181	31.3897	36.2111	36.2111	40.5045	55.6714	65.5223

The continuous rotation of the site rows discussed above leads to the formation of the cylindrical carbon tube. In the case of the prismatic tube, its individual faces have a constant tilting angle with respect to the electron beam. Therefore, the electron diffraction pattern of the faceted tube exhibits a discrete set of lattice orientations with respect to the tube axis rather than a continuous rotation of the lattice. This corresponds to the reflections, the arrangement of which is determined by the set of inclined cross-sections of the site rows parallel to the *c** axis corresponding to the given prismatic tube. Let the site rows of the face perpendicular to the electron beam and those in the tilted face form angle φ (see the right top panel in Fig. 2). Consider reflections *Y* and *Y*' located in the perpendicular plane (they are shown in the electron diffraction pattern in the left top part of Fig. 2). They are split due to the nonzero chirality and the angle between their radius-vectors is equal to $2\alpha_n$ (Fig. 2, lower panel), where α_n is the chirality angle, and the length of the radius vector for each reflection is equal to r_{hk}. In the tilted plane, these reflections correspond to reflections *X* and *X*', with the radius vector $\frac{r_{hk}}{\cos\phi}$ (ϕ is the angle between the radius vector of the reflection and its projection onto the perpendicular plane, $0 \le \phi \le \varphi$). The change in the length of the radius vector r_{hk} of the reflection depends on the angle ϕ. Hence, the tilting of the face gives rise to changes in the interplanar distances d_{hkl} along symmetrically equivalent directions. Undistorted d_{hkl} should be located at the tilting axis, whereas the maximum distortions should correspond to the direction perpendicular to the tilting axis.

The tilting of the tube face causes changes not only in the distances between reflections but also in the angles between radius vectors of the reflections. Let us now demonstrate how the chirality angle α_t in the tilted plane changes as compared to the chirality angle α_n in the perpendicular plane (Fig. 2, bottom). Taking into account the prismatic symmetry of the faceted tubes, we can base our consideration on the fact that the tilting direction should be parallel to the tube axis.

Let θ be the angle between the tilting axis and the radius vector of the split reflection in the tilted plane and θ' be the angle between the tilting axis and the projection of the radius vector corresponding to the split reflection onto the perpendicular plane. In this notation, we have

$$\theta = (90^\circ - \alpha_t), \quad \theta' = (90^\circ - \alpha_n).$$

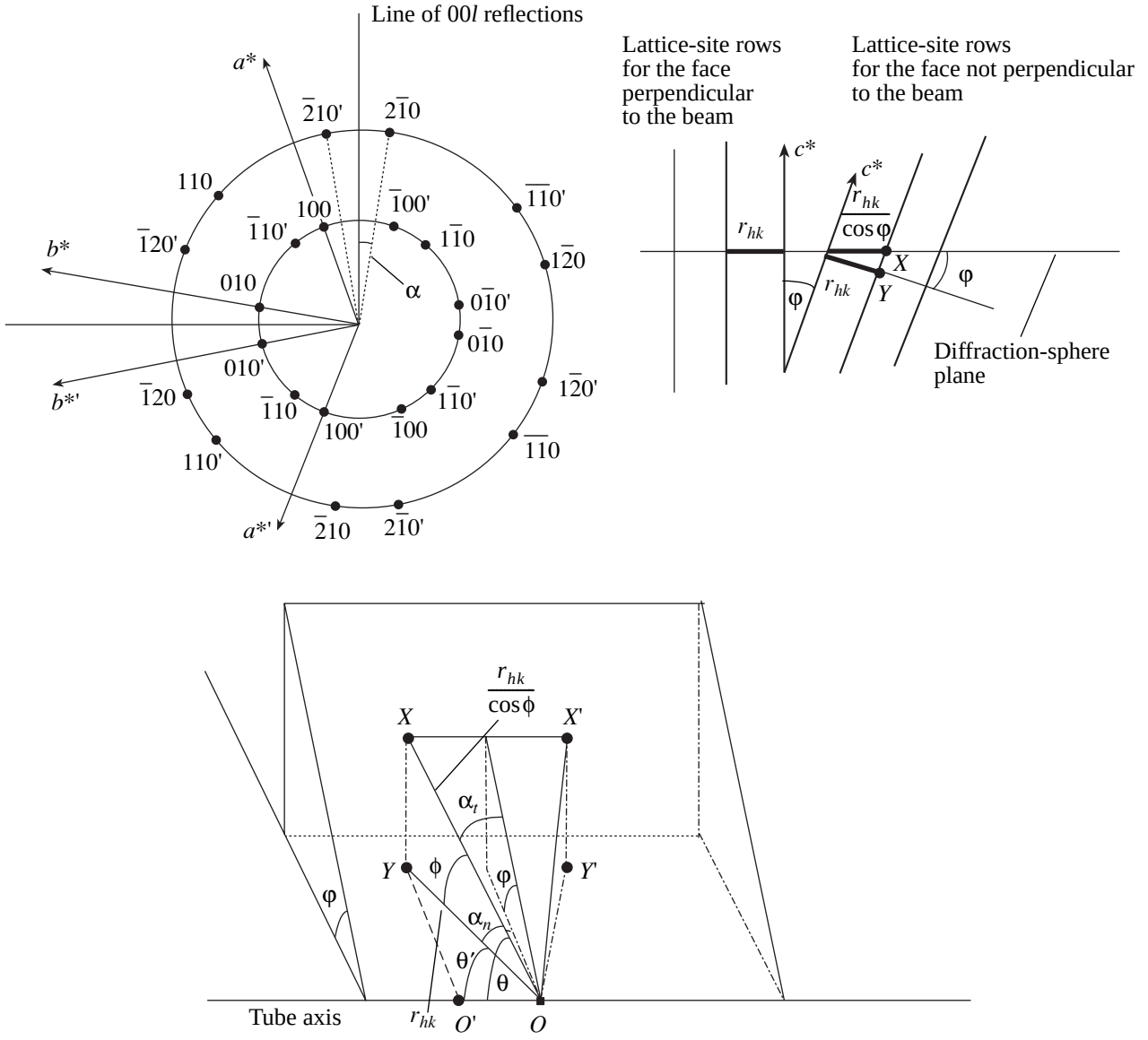

Fig. 2. Left upper panel: the schematic electron diffraction pattern for the tube with nonzero chirality. Split reflections $(\bar{2}10)'$ and $(2\bar{1}0)$, α is the chirality angle. Right upper panel: the positions of lattice-site rows for the faceted tube (for two faces) and their cross-section by the diffraction-sphere plane. The change in interplanar distances determined by the parameter r_{hk} is shown for a tilted face in comparison with the face perpendicular to the electron beam. Lower panel: the schematic diagram illustrating calculations of the chirality angle for the tube with faces; α_n is the chirality angle, i.e., the half angle between the radius vectors of reflections *Y* and *Y*' (in the zero-slope *a***b** plane) and α_t is the distorted chirality angle, i.e., the half angle between the radius vectors of the *X* and *X*' reflections (in the tilted plane).

Let us relate θ' and θ

$$\tan\theta' = \frac{YO'}{OO'} = \frac{XO'\cos\varphi}{OO'} = \tan\theta\cos\varphi.$$

Therefore,

$$\tan(90^\circ - \alpha_n) = \tan(90^\circ - \alpha_t)\cos\varphi. \qquad (1)$$

Relationship (1) should be taken into account in measurements of the chirality angle in a faceted tube: if the measurements are performed using *X* and *X*' reflections coming from the face tilted with respect to the beam, then the chirality angle turns out to be distorted (α_t) compared to the chirality angle α_n in the perpendicular plane.

Let us discuss the electron diffraction pattern of a multiwall tube 190 nm in diameter, which is represented in Fig. 3 [2]. Measurement of the chirality angle between the radius vectors of $(\bar{2}10)'$ and $(2\bar{1}0)$ reflections gives the value $\alpha = 25.1^\circ$ (±0.3°) [2]. However, if

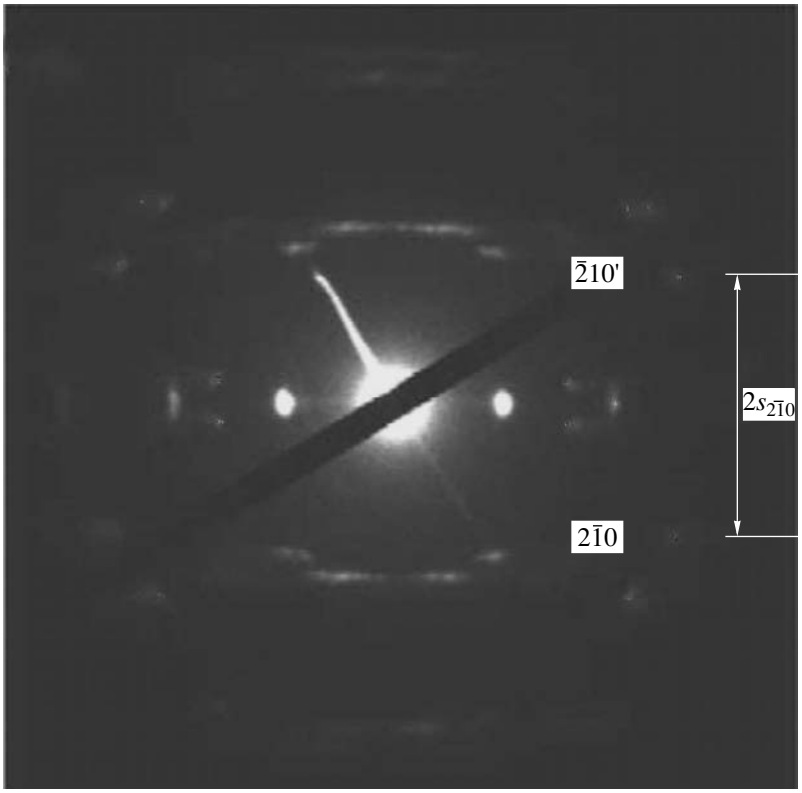

Fig. 3. Electron diffraction pattern for a multiwall monochiral carbon tube [2]. Doubled $s_{2\bar{1}0}$ distance is indicated; in electron diffraction pattern, this represents the parameter $S_{2\bar{1}0}$.

we calculate the interplanar distance d_{110} using $(\bar{2}10)'$ and $(2\bar{1}0)$ reflections, it turns out to be 1.17 Å (±0.2 Å), which is close to the tabulated point d_{112} = 1.1529 Å, rather than to the tabulated value d_{110} = 1.2280 Å. This deviation indicates that the reflections come from the face that is not perpendicular to the beam (in this case, the tilting angle corresponding to the rotation of the (11*l*) row is equal to 36.2°, according to the aforementioned data). Therefore, the chirality angle α_t obtained using this pair of reflections will deviate from the true one.

Let us discuss the problem concerning the determination of the chirality angle for the non-cylindrical tube. The reflections that arise due to the rotation of one site row and that correspond to the faces with different tilting angles with respect to the beam lie at one ray parallel to the equatorial line of the electron diffraction pattern. Therefore, it would be convenient to relate the chirality angle not to those reflections whose positions at the ray vary depending on the tilt of the face with respect to the beam, but to the position of the ray where all these reflections lie.

In paper [3], we considered the problem of describing the positions of the reciprocal lattice sites of the tube as a function of the chirality angle. To this end, we introduced coordinate S_{hk0} (α), which is defined by Eq. (2) and represents the distance between the point of origin for the coordinate system to the plane that is perpendicular to the axis of rotation and passes through the given site (Fig. 1, bottom):

$$S_{hk0} = \left| \frac{h}{a\sin\gamma}\cos(\gamma^* + \alpha) + \frac{k}{b\sin\gamma}\cos\alpha \right|, \qquad (2)$$

where a and b are the lengths of the basis vectors **a** and **b** with angle $\gamma = 120°$ between them, $a = b = 2.46$ Å, γ^* is the angle between **a*** and **b***, $\gamma^* = 180° - \gamma = 60°$, h and k are the indices of reflection in the a^*b^* plane, and α is the chirality angle of the tube. As was shown above, the set of reflections arising due to the rotation of the site row (*hkl*) lies on the ray that starts from reflection (*hk*0) and is perpendicular to the rotation axis of the tube (Fig. 1, bottom). Therefore, the position of the ray at which the reflection (*hk*0) lies could also be given by the coordinate S_{hk0} (α), which is a single-valued function of the chirality angle.

Now, we determine the chirality angle for the electron diffraction pattern shown in Fig. 3 using the parameter S_{hk0} for the rays at which reflections $(2\bar{1}0)$ and $(\bar{2}10)'$ lie. The latter reflections are used in the conventional technique for finding the chirality angle. We

calculate the constant C of the electron microscope using the relationship $r(\text{mm}) = R(\text{Å}^{-1})C$ (Å mm) for the electron diffraction pattern based on the reflections of the {100} family. Here, we assumed that $R(\text{Å}^{-1}) = S_{2\bar{1}0}(\text{Å}^{-1})$ and $r(\text{mm}) = s_{2\bar{1}0}$ (mm). As a result, we found the value 0.359 Å^{-1} for $S_{2\bar{1}0}$ and, according Eq. (2), the chirality angle is equal to $\alpha = 26.5°$ (with a measurement error of ±0.1°).

Thus, the difference in the values of the chirality angle calculated on the basis of relationship (2) and determined in [2] is equal to 1.4°. How significant is this difference for the properties of the carbon nanotube? According to the calculations reported in [4], the electronic characteristics of the tube of the given radius in the single-wall approximation could be determined through the chirality of the tube expressed in terms of the index k, which incorporates the indices m and n characterizing chirality as

$$k = m - 2n \ (m \geq 2n).$$

Note that if $k = 0$, the tube is characterized by metallic conductivity; if $k = 3(q + 1) = (3, 6, 9, \ldots)$, the tube is a narrow-band semiconductor ($q = 0, 1, 2, 3$); if $k = 3q + 2 = (2, 5, 8, \ldots)$ or $k = 3q + 1 = (1, 4, 7, \ldots)$, the tube is a semiconductor with a medium value of band gap. For the tube under study, we have $k = 411$; thus, in the single-wall approximation, this tube is a narrow-band semiconductor. We use formulas relating the tube diameter D and the chirality angle α to indices m and n characterizing chirality

$$D = \sqrt{m^2 + n^2 - mn}\frac{d_0\sqrt{3}}{\pi},$$

where $d_0 = 1.42$ Å,

$$\tan\alpha = \frac{n\sqrt{3}}{2m - n}.$$

The increase in k by one changes the electronic properties of the tube from a narrow-band semiconductor to a semiconductor with a medium value of band gap. The increase in k by one implies the increase in m by one (at n = const). In the tube with a diameter of 190 nm and a chirality angle of 25.1°, this leads to a change in the chirality angle by 0.07°.

Thus, we have demonstrated that continuous rotation of the crystal lattice in the case of a cylindrical tube gives rise to a set of reflections in the electron diffraction pattern, which merge into rays (bars) for high-order reflections. In the case of a prismatic tube, the set of reflections correspond to a certain rotation angle of lattice-site rows parallel to the c^* axis with respect to the rotation angle. It is shown that measurement of chirality angle based directly on electron diffraction patterns as an angle between radius vectors split due to nonzero chirality can lead to erroneous results when the tube shape deviates from the cylindrical one [according to Eq. (1)]. We suggested a technique for calculating the chirality angle of a graphite tube taking into account deviation from the cylindrical shape of the tube. The results of calculations by Eq. (2), as well as estimates of the sensitivity of electronic characteristics of the tube to changes in the chirality angle, demonstrate that it is necessary to calculate chirality angle with the inclusion of the tilting of the tube face with respect to the electron beam. Calculations of chirality angle based on Eq. (2) with the use of coordinate S_{hk0} could be applied to determine chirality angle without a preliminary analysis of the structural features of tube walls. This is possible because chirality angle is calculated using the positions of the rays along which displacements from the standard positions occur due to the structural features of tube walls rather than on the basis of the positions of separate reflections undergoing these displacements. Calculation of chirality angle based on the position of rays (2) rather than on the angle between radius vectors of separate reflections apparently is a correct method for determining the chiral characteristics not only of prismatic tubes, but also of the tubes of more complicated cross-section (e.g., of column-shaped tubes [5]).

REFERENCES

1. L. A. Bursill, J.-L. Peng, and X.-D. Fan, Philos. Mag. **71**, 1161 (1995).
2. W. Ruland, A. K. Schaper, *et al.*, Carbon **41**, 423 (2003).
3. L. D. Grigor'eva, Dokl. Akad. Nauk **396** (1), 35 (2004) [Dokl. Phys. **49**, 261 (2004)].
4. H. Yorikawa and S. Muramatsu, Phys. Rev. B **50** (16), 12203 (1994).
5. B. Q. Wei and Z. J. Zhang, Carbon **40**, 47 (2002).

Translated by K. Kugel

Doklady Physics, Vol. 50, No. 3, 2005, pp. 128–131. Translated from Doklady Akademii Nauk, Vol. 401, No. 3, 2005, pp. 329–332.

PHYSICS

Revision of the Theory of Energetic-Particle Modes in Tokamaks

A. B. Mikhaĭlovskiĭ[1,2], E. A. Kovalishen[1,2], S. V. Konovalov[1,3], and M. S. Shirokov[1,4]

Presented by Academician A.M. Fridman October 13, 2004

Received October 22, 2004

The investigation of instabilities driven by fast ions in tokamaks represents one of the central problems of the physics of collective processes in magneto-thermonuclear reactors. This area of physics has been developed in view of the design of the International Thermonuclear Experimental Reactor (ITER) [1]. In the framework of such an investigation, a class of instabilities called "energetic-particle modes" was predicted in [2–6], whose authors stated that energetic ions not only drive these modes but are also responsible for their existence. In this work, we show that the theory of energetic-particle modes is invalid, because it is based on electrodynamic equations that disregard the effect of the drift of electrons in crossed fields, which compensate the electric charge of energetic ions. This effect was initially taken into account in [7], and its physical meaning was explained in [8], where it was noted that the effect under discussion is physically similar to the Varma–Shukla effect studied in the physics of dusty plasma [9].

As was mentioned in [4], energetic-particle modes are negative-energy waves. At the same time, according to the general concepts [10], such waves can exist only if the contribution of energetic ions to the equation for perturbations is not small as compared to other terms of this equation. We show that, in the approximation of large orbits of energetic particles, which is used in the theory of energetic-particle modes [2–6], their contribution represents a small addition compared to the contribution of compensating electrons. For this reason, the existence of negative-energy waves in the case under consideration is impossible.

The problem of perturbations in reversed (negative) shear discharges was considered in [7, 8]. For this reason, we study the case of positive-shear discharges (a monotonic profile of the safety factor). In this case, a new class of perturbations called compensating-electron Alfvén eigenmodes is realized. Compensating-electron Alfvén eigenmodes, as well as nonexisting energetic-particle modes, lie in the so-called Alfvén continuum. As a result, they are sensitive to continuum dissipation (cf. [2–6]). However, in contrast to energetic-particle modes, compensating-electron Alfvén eigenmodes are positive-energy waves. Therefore, continuum dissipation leads to their damping. According to the above discussion, the contribution of energetic ions to the equation for compensating-electron Alfvén eigenmodes is a small correction. This correction is complex, and its imaginary part characterizes the effect of resonance interaction of energetic ions with compensating-electron Alfvén eigenmodes. We show that compensating-electron Alfvén eigenmodes propagate in a direction opposite to that of the diamagnetic drift of energetic ions. Hence, according to general concepts of the theory of plasma instabilities (see [11] and references cited therein), the mentioned resonance interaction leads to additional damping of compensating-electron Alfvén eigenmodes. Overall, the general pattern of Alfvén instabilities in discharges with the monotonic profile of the safety factor is favorable to that predicted by the theory of energetic-particle modes.

We assume that, in addition to the thermal plasma characterized by equilibrium ion density n_c, there are energetic ions with an equilibrium density of n_h. In this case, the equilibrium density of electrons is equal to the sum $n_c + \frac{n_h e_h}{e_i}$, where e_h and e_i are the charges of energetic and thermal ions, respectively, under the assumption that $e_i \equiv e = -e_e$. Electrons with a density of $\frac{n_h e_h}{e_i}$ are called compensating electrons.

[1] *Institute of Nuclear Fusion, Russian Research Center Kurchatov Institute, pl. Akademika Kurchatova 1, Moscow, 123182 Russia*
e-mail: mikh@nfi.kiae.ru

[2] *Laboratory of Nonlinear Physics, Moscow Institute of Physics and Technology, Institutskiĭ per. 9, Dolgoprudnyĭ, Moscow region, 141700 Russia*

[3] *Naka Fusion Research Establishment, Japan Atomic Energy Research Institute, Ibaraki 3111 0193, Japan*

[4] *Department of Plasma Physics, Moscow Engineering Physics Institute (State University), Kashirskoe sh. 31, Moscow, 115409 Russia*

1028-3358/05/5003-0128$26.00

According to [8], in the approximation of infinitely large orbits of energetic ions, the perturbed current-closure equation, in which the drift of compensating electrons in crossed fields is taken into account, is reduced to the form

$$\frac{d}{dr}\left[\left(\frac{\omega^2}{v_A^2}-k_\parallel^2\right)\frac{d\phi}{dr}\right]-k_y^2\left(\frac{\omega^2}{v_A^2}-k_\parallel^2\right)\phi + \frac{4\pi e_h\omega k_y}{cB_0}\frac{dn_h}{dr}\phi = 0. \quad (1)$$

Here, r is the radial coordinate; ω is the frequency of perturbations [the time dependence of perturbations is taken in the form $\exp(-i\omega t)$]; v_A is the Alfvén velocity; $k_\parallel = \left(\frac{m}{q} - n\right)/R$, m and n are the poloidal and toroidal mode numbers, respectively; $q = q(r)$ is the safety factor; R is the large radius of the torus; ϕ is the perturbed electrostatic potential; $k_y = \frac{m}{r}$, B_0 is the equilibrium magnetic field; and c is the speed of light. The substitution of $\frac{d}{dr} \longrightarrow ik_x$, where k_x is the radial wavenumber, into Eq. (1) yields the local dispersion equation

$$\frac{k_\parallel^2 c^2}{\omega^2}-\frac{c^2}{v_A^2}-\varepsilon_{11}^{e,h} = 0. \quad (2)$$

Here, $\varepsilon_{11}^{e,h}$ is the transverse permittivity of compensating electrons, given by

$$\varepsilon_{11}^{e,h} = -\frac{4\pi e_h k_y c}{k_\perp^2 B_0\omega}\frac{dn_h}{dr}, \quad (3)$$

where $k_\perp^2 = k_x^2 + k_y^2$.

According to the above discussion, we consider a monotonic profile q. In this case, $k_\parallel = -\frac{k_y s x}{qR}$, where s is the shear and x is the distance from the rational magnetic surface near which perturbation is localized. In the local approach, we can set $k_\perp^2 x^2 \longrightarrow \frac{1}{4}$. Then, neglecting the term with $\frac{c^2}{v_A^2}$ (inertia term) in Eq. (2), we obtain the following "local" expression for the eigenfrequency

$$\omega = \omega_{CE}. \quad (4)$$

Here,

$$\omega_{CE} \equiv -\frac{1}{4}\frac{k_y\omega_A^2}{\Omega_h\kappa_h}\frac{n_c M_c}{n_h M_h}, \quad (5)$$

where $\kappa_h \equiv \frac{d\ln n_h}{dr}$, $\omega_A = \frac{s v_A}{qR}$, subscript CE means compensating electrons, Ω_h is the cyclotron frequency of energetic ions, and M_h and M_c are the masses of energetic and thermal ions, respectively. Below, expression (5) for eigenfrequency will be corroborated and refined in the eigenvalue problem. Eigenmodes characterized by this frequency are the compensating-electron Alfvén eigenmodes introduced above. Using Eq. (15.16) from [12] and taking Eq. (3) into account, one can see that compensating-electron Alfvén eigenmodes are positive-energy waves.

When the contribution of energetic ions is taken into account, Eq. (2) is modified by the change

$$\varepsilon_{11}^{e,h} \longrightarrow \varepsilon_{11}^{h} \equiv \varepsilon_{11}^{e,h} + \varepsilon_{11}^{i,h}, \quad (6)$$

where $\varepsilon_{11}^{i,h}$ is the permittivity of energetic ions. An expression corresponding to the approximation of strongly circulating Maxwell energetic ions with nonuniform density n_h and uniform temperature T_h can be used as a model for $\varepsilon_{11}^{i,h}$. In this case, we have (for details, see [11, 13])

$$\varepsilon_{11}^{i,h} = \frac{1}{k_\perp^2 d_h^2}\left[1-\left(1-\frac{\omega_{*h}}{\omega}\right)\delta_h\right]. \quad (7)$$

Here,

$$\delta_h = \langle J_0^2(\xi_{\perp h})\rangle + \frac{1}{\omega}\sum_{p=-\infty}^{\infty}\left\langle \frac{J_0^2(\xi_{\perp h})J_p^2(\xi_{\parallel h})\left(\frac{p v_\parallel}{qR}\right)^2}{\omega - k_\parallel v_\parallel - \frac{p v_\parallel}{qR}}\right\rangle, \quad (8)$$

$\omega_{*h} = \frac{k_y c T_h \kappa_h}{e_h B_0}$ is the diamagnetic drift frequency of energetic ions, $\xi_{\perp h} = \frac{k_\perp v_\perp}{\Omega_h}$, $\xi_{\parallel h} = k_\perp\Lambda$, where

$$\Lambda = q\left(\frac{v_\perp^2}{2} + v_\parallel^2\right)(\Omega_h v_\parallel)^{-1}$$

is the radial width of the magnetic-drift orbits of energetic ions, where $v_\perp$ and $v_\parallel$ are the transverse and longitudinal velocity of particles, respectively. Angle brackets represent averaging with the Maxwell distribution of energetic ions and d_h is the Debye radius of energetic ions. The term with $\frac{1}{k_\perp^2 d_h^2}$ corresponds to the Boltzmann response of energetic ions. The term with $\langle J_0^2(\xi_{\perp h})\rangle$ can be called the cylindrical nonadiabatic response of energetic ions, and the term with $J_0^2(\xi_{\perp h})J_p^2(\xi_{\parallel h})$ describes their toroidal response.

The case $\omega \ll \omega_{*h}$ is the most important for the problem of instabilities. In this case, the expression for ε_{11}^h determined by Eq. (6) takes the form

$$\varepsilon^h = \varepsilon^{e,h}(1-\delta_h). \tag{9}$$

In terms of ε^h, it can be shown that analysis in [2–6] is based on the use of an expression of type (9), where unity on the right-hand side is neglected compared to δ_h. However, in the case $(k_\perp\rho_h, k_\perp\Lambda_h) \gg 1$ considered in those works, Eq. (8) shows that

$$\delta_h \ll 1. \tag{10}$$

In other words, the term with δ_h is a small addition on the right-hand side of Eq. (9), which contradicts works [2–6].

We now consider the resonance interaction of energetic ions with compensating-electron Alfvén eigenmodes. Using Eqs. (2), (6), and (9) and neglecting the inertial term as stated above, we arrive at the local dispersion equation

$$1 - \frac{\omega}{\omega_{CE}}(1-\delta_h) = 0. \tag{11}$$

We seek a solution of Eq. (11) in the form $\omega = \omega_{CE} + i\omega_I^h$, where ω_I^h is the imaginary part of the mode frequency that is associated with the imaginary part of δ_h, so that $\omega_I^h = \omega_{CE}\mathrm{Im}\delta_h$. Taking Eq. (8), we have the identity

$$\frac{1}{\omega - k_\parallel v_\parallel - \dfrac{pv_\parallel}{qR}} = \frac{P}{\omega - k_\parallel v_\parallel - \dfrac{pv_\parallel}{qR}} - i\pi\delta\left(\omega - k_\parallel v_\parallel - \frac{pv_\parallel}{qR}\right), \tag{12}$$

where P means the principal value. Then, it follows from Eq. (8) that $\mathrm{Im}\delta_h \sim -\mathrm{sgn}\,\omega$. As a result, we find that $\omega_I^h < 0$, which corresponds to the damping of the mode. Such a result could have been predicted in advance, taking into account that the modes under consideration have positive energy and propagate in a direction opposite to that of the diamagnetic drift velocity $\dfrac{\omega}{\omega_{*h}} < 0$.

For slightly circulating or trapped energetic ions, a specific expression for δ_h evidently differs from Eq. (8). Nevertheless, the above condition of the negativity of $\mathrm{Im}\delta_h$ remains unchanged. Therefore, the conclusion that energetic ions lead to damping is fairly universal. In order to ascertain this fact, one is advised to see [14] (see also Section 4.3.3 in [13]), where the interaction of Alfvén waves with strongly trapped ions was investigated.

Taking the local approach to the eigenvalue problem, we note that, in the case of the monotonic profile of the safety factor, differential equation (1) takes the form

$$\frac{d}{dx}\left[\left(\frac{\omega^2}{\omega_A^2 k_y^2} - x^2\right)\frac{d\phi}{dx}\right] - k_y^2\left(\frac{\omega^2}{\omega_A^2 k_y^2} - x^2\right)\phi - Q_h\phi = 0, \tag{13}$$

where

$$Q_h = -\frac{\omega\Omega_h\kappa_h n_h M_h}{k_y\omega_A^2 n_c M_c}. \tag{14}$$

The above local analysis concerned the limiting case of zero $\dfrac{\omega^2}{\omega_A^2}$, which represents a complete neglect of the inertia of the plasma. In this case, Eq. (13) reduces to the form

$$\frac{d}{dx}\left(x^2\frac{d\phi}{dx}\right) - k_y^2 x^2\phi + Q_h\phi = 0. \tag{15}$$

This equation has an exact solution expressed in terms of the Bessel function $K_{i\alpha}(|xk_y|)$ of an imaginary argument (for details, see Section 5 in [15]), where

$$\alpha = \left(Q_h - \frac{1}{4}\right)^{1/2}. \tag{16}$$

Following [15], one can find the explicit asymptotic behavior of the solution of Eq. (15) for $xk_y \ll 1$, which can be called the short-range asymptotic behavior of the inertialess solution.

At the same time, in the region $x \simeq \dfrac{\omega}{\omega_A k_y}$, where the inertia term in Eq. (13) is important, neglecting the term with k_y^2 when $\dfrac{\omega^2}{\omega_A^2}$ is small, we reduce Eq. (13) to the form

$$\frac{d}{dz}\left[(1-z^2)\frac{d\phi}{dz}\right] + \nu(\nu+1)\phi = 0, \tag{17}$$

where $z = \dfrac{xk_y\omega_A}{\omega}$ and $\nu = -\dfrac{1}{2} + i\alpha$. Equation (17) has a solution that is expressed in terms of Legendre functions. This solution is complex due to the presence of singularities $z = \pm 1$ in Eq. (17). This circumstance leads to the necessity of bypassing singularities in accordance with the well-known Landau rule. The fact that the solution of Eq. (17) is complex physically presents the continuum dissipation discussed above.

Finding the solution of Eq. (17), we can determine its asymptotic behavior for large z values, which can be called the large-range asymptotic behavior. Joining this asymptotic behavior with the aforementioned short-

range asymptotic behavior of the inertialess solution, we arrive at the dispersion equation

$$\frac{\omega}{\omega_A} = 16\exp\left(-\frac{\pi l}{\alpha} - \gamma \pm \frac{\pi}{2} + \frac{i\pi}{2}\operatorname{sgn}\omega\right), \quad (18)$$

where $l = 1, 2, 3, \ldots$ is the number of the mode level and γ is the Euler constant.

Dispersion equation (18) is obtained under the conditions $\alpha \ll 1$ and $\operatorname{Re}\alpha \gg \operatorname{Im}\alpha$. The latter condition is satisfied only if Q_h exceeds a threshold value of $\frac{1}{4}$:

$$Q_h > \frac{1}{4}. \quad (19)$$

The condition $\alpha \ll 1$ is evidently satisfied only if inequality (19) is weak. An additional analysis shows that compensating-electron Alfvén eigenmodes also exist when inequality (19) is quite strong.

According to Eq. (18), the frequency of compensating-electron Alfvén eigenmodes is complex, i.e.,

$$\omega = \omega_R + i\omega_I^{CD}, \quad (20)$$

where

$$\omega_R = \omega_{CE}\left\{1 + \frac{4\pi^2 l^2}{\left[\ln\frac{16\omega_A}{\omega_{CE}}\right]^2}\right\}, \quad (21)$$

$$\omega_I^{CD} = -4\pi^3|\omega_{CE}|\frac{l^2}{\left[\ln\frac{16\omega_A}{\omega_{CE}}\right]^3}. \quad (22)$$

According to Eq. (20), the imaginary part of the eigenfrequency of compensating-electron Alfvén eigenmodes is negative. This property confirms the above conclusion that continuum dissipation leads to the damping of compensating-electron Alfvén eigenmodes. It is seen that decrement increases as l^2 with the level number l. Therefore, modes with the minimum l value, $l = 1$, are most interesting for instabilities.

ACKNOWLEDGMENTS

This work was supported by the Russian Foundation for Basic Research (project no. 03-02-16294); the Council of the President of the Russian Federation for Support of Young Russian Scientists and Leading Scientific Schools (project no. NSh-2024.2003.2); the Department of Atomic Science and Technology, the Ministry of Atomic Industry of the Russian Federation; and the US Civilian Research and Development Foundation for the Independent States of the Former Soviet Union (grant no. BRHE REC-011).

REFERENCES

1. ITER Physics Expert Group on Energetic Particles, Heating and Current Drive, ITER Physics Basis Editors, and ITER EDA, Nucl. Fusion **39**, 2471 (1999).
2. S. T. Tsai and L. Chen, Phys. Fluids B **5**, 3284 (1993).
3. L. Chen, Phys. Plasmas **1**, 1519 (1994).
4. F. Zonca and L. Chen, Phys. Plasmas **3**, 323 (1996).
5. F. Zonca and L. Chen, Phys. Plasmas **7**, 4600 (2000).
6. F. Zonca, S. Briguglio, L. Chen, *et al.*, Phys. Plasmas **9**, 4939 (2002).
7. H. L. Berk, D. N. Borba, B. N. Breizman, *et al.*, Phys. Rev. Lett. **87**, 185002 (2001).
8. S. E. Sharapov, A. B. Mikhailovskii, and G. T. A. Huysmans, Phys. Plasmas **11**, 2286 (2004).
9. S. V. Konovalov, A. B. Mikhailovskii, V. S. Tsypin, and S. E. Sharapov, Dokl. Phys. **47**, 488 (2002).
10. B. B. Kadomtsev, A. B. Mikhailovskii, and A. V. Timofeev, Zh. Éksp. Teor. Fiz. **47**, 2266 (1964) [Sov. Phys. JETP **20**, 1517 (1964)].
11. A. B. Mikhailovskii and A. M. Fridman, Nucl. Fusion **16**, 837 (1976).
12. V. D. Shafranov, Rev. Plasma Phys. **3**, 1 (1967).
13. A. B. Mikhailovskii, Rev. Plasma Phys. **9**, 103 (1986).
14. T. D. Kaladze and A. B. Mikhailovskii, Nucl. Fusion **17**, 411 (1977).
15. A. B. Mikhailovskii, *Instabilities in a Confined Plasma* (Institute of Physics, Bristol, 1998).

Translated by R. Tyapaev

Doklady Physics, Vol. 50, No. 3, 2005, pp. 132–135. Translated from Doklady Akademii Nauk, Vol. 401, No. 2, 2005, pp. 185–188.

TECHNICAL PHYSICS

Failure of Concrete and Reinforced-Concrete Plates under High-Speed Shock and Explosion

S. A. Afanas'eva, N. N. Belov, D. G. Kopanitsa, N. T. Yugov, and A. A. Yugov

Presented by Academician G.G. Chernyĭ October 14, 2004

Received October 20, 2004

It is well known that numerous studies have been devoted to calculating collisions between solids and various targets (e.g., monolithic, layered, layered-separated targets) made of metals and composite materials (see review in [1]). Nevertheless, problems associated with the piercing of concrete and reinforced-concrete structures remain insufficiently studied. In [2], experimental and theoretical data are presented that relate to shock interactions between cylindrical bodies and reinforced-concrete plates. The corresponding calculation was performed under assumption of the absolute rigidity of a reinforcing fabric and a striker. In this case, the striker diameter was supposed to be smaller than the fabric-cell size. These assumptions are not always adequate for addressing practical problems. In the same study [2], the conclusion was drawn that reinforcing a concrete obstacle improves its bearing strength but does not noticeably affect the process of striker penetration.

Recently, a mathematical model [3] was proposed that describes the deformation and failure of layered concrete structures under a high-speed shock. This model makes it possible to account for the existence of reinforcing steel bars in a reinforced-concrete plate and does not impose any constraints on characteristic sizes of interacting bodies. However, certain difficulties can arise in the process of the numerical realization of this problem. We suggest the necessity of a small-size spatial and temporal step resulting in time-consuming calculations.

In the present study, the mathematical model of [3] is generalized for calculation of the deformation and failure of reinforced concrete subjected to shock-wave loading. The reinforced concrete as a concrete layer containing a steel reinforcing fabric is modeled by an elastoplastic medium, i.e., by an homogeneous two-phase mixture of steel and concrete. The initial density ρ_{s0} of the reinforced concrete is determined by the formula $\rho_{s0} = \nu_1\rho_0 + \nu_2\rho_{20}$, where ρ_{10}, ρ_{20} and ν_1 and ν_2 are the initial densities and concentrations of steel and concrete, respectively ($\nu_1 + \nu_2 = 1$). The volume concentrations are determined via areas occupied by steel and concrete in the cross section perpendicular to the direction of a reinforcing bar: $\nu_1 = \dfrac{\pi d_1 n}{4L}$, $\nu_2 = 1 - \nu_1$, where n is the number of bars in a strip of length L, and d_1 is bar diameter (Fig. 1).

The set of equations describing the motion of a porous elastoplastic medium is of the form

$$\frac{d}{dt}\int_V \rho dV = 0, \quad \frac{d}{dt}\int_V \rho \mathbf{u} dV = \int_R \boldsymbol{\sigma}_n dR + \int_V \rho \mathbf{F} dV,$$

$$\frac{d}{dt}\int_V \rho E dV = \int_V \sigma_{ij} e_{ij} dV,$$

$$2\mu\left(e_{ij} - \frac{1}{3}e_{kk}\delta_{ij}\right) = \frac{dS_{ij}}{dt} + -S_{ik}\omega_{jk} - S_{jk}\omega_{ik} + \lambda S_{ij},$$

$$\frac{d\alpha}{dt} = -\frac{(\alpha_0 - 1)^{2/3}}{\eta}\alpha(\alpha - 1)^{1/3}\Delta p,$$

where,

$$\Delta p = p + \frac{a_s}{\alpha}\ln\frac{\alpha}{\alpha - 1} \text{ at } \Delta p < 0, \ \alpha < \alpha^*,$$

$$\Delta p = p - \frac{2}{3}\frac{\sigma_{sm}}{\alpha}\ln\frac{\alpha}{\alpha - 1} \text{ at } \Delta p > 0, \ \alpha_0 < \alpha,$$

$$\mu = \frac{\mu_m}{\alpha}\left[1 - \frac{6K_m + 12\mu_m}{9K_m + 8\mu_m}\frac{\alpha - 1}{\alpha}\right].$$

Here, $\rho = \dfrac{\rho_m}{\alpha}$ and ρ_m are the densities of the medium and of the matrix, respectively; $\mathbf{u}$ is the velocity vector; $\boldsymbol{\sigma}_n$ is the vector of exterior surface stresses; $\mathbf{F}$ is the vec-

Tomsk State University,
pr. Lenina 50, Tomsk, 634050 Russia
e-mail: svetl@niipmm.tsu.ru; kopanitsa@niipmm.tsu.ru

1028-3358/05/5003-0132$26.00

tor density of exterior mass forces; E is the internal energy per unit mass; $\sigma_{ij} = S_{ij} - P\delta_{ij}$ are the stress-tensor components; S_{ij} are the components of the stress-tensor deviator, δ_{ij} is the Kronecker delta; p is hydrostatic pressure; $e_{ij} = 0.5(\nabla_i u_j + \nabla_j u_i)$ are the strain-rate tensor components; u_i are the velocity-vector components; μ_m is the matrix shear modulus; σ_{sm} is the matrix dynamic yield strength; $K_m = \rho_0 c_0^2$ is the bulk matrix compression modulus; $\alpha = \dfrac{1}{1-\xi}$ is the porosity; ξ is the relative void volume; and ρ_0, c_0, α_0, α^*, η and a_s are constants of the material.

The parameter λ is zero and always positive in the case of the elastic and plastic strains, respectively. This parameter is determined by the Mises yield condition

$$S_{ij}S_{ij} = \frac{2}{3}\left(\frac{\sigma_{sm}}{\alpha}\right)^2.$$

The shear modulus and the dynamic yield strength for reinforced concrete can be expressed in terms of the corresponding parameters of the mixture components:

$$\mu_m = \frac{1}{\sum_{i=1}^{2}\dfrac{\nu_i}{\mu_{0i}}}, \quad \sigma_{sm} = \sum_{i=1}^{2} m_i\sigma_{si},$$

where $m_i = \dfrac{\nu_i\rho_{i0}}{\rho_{s0}}$ are the mass concentrations of steel ($i = 1$) and concrete ($i = 2$) in the reinforced-concrete layer ($m_1 + m_2 = 1$); and μ_{0i} and σ_{si} are the shear moduli and yield strengths for steel and concrete, respectively.

The equation of state for reinforced concrete is of the form

$$p = \frac{\rho_{s0}c_0^2\left(1 - \dfrac{\gamma_s\eta_0}{2}\right)\eta_0}{(1-q\eta_0)^2} + \gamma_s\rho_{s0}E, \qquad (1)$$

where $\eta_0 = 1 - \rho_{s0}v$, v is the specific volume. The Grüneisen coefficients γ_{i0} for steel and concrete are

$$\gamma_s = \frac{v_{s0}}{\sum_{i=1}^{2} m_i v_{0i}\gamma_{i0}^{-1}},$$

where $v_{s0} = \dfrac{1}{\rho_{s0}}$.

The coefficients c_0 and q in the linear dependence of the shock-wave velocity on the mass velocity of reinforced concrete are determined by the shock adiabats $D_i = c_{i0} + q_i u_i$ of components of the steel–concrete mixture in the following manner.

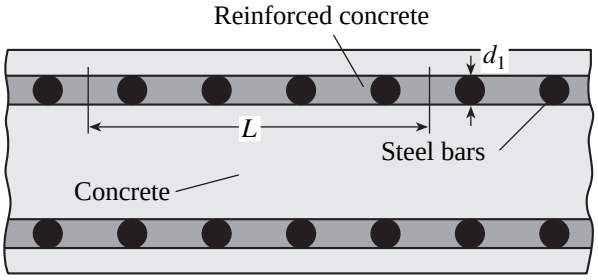

Fig. 1. Sketch of reinforced concrete.

In terms of the variables (v, p), the shock adiabat of the steel–concrete mixture has the form

$$v(p) = \sum_{i=1}^{2} m_i\left\{v_{i0} - \frac{1}{p}\left[\frac{c_{i0}}{q_i}\sqrt{\frac{p}{\rho_{i0}c_{i0}^2} + \frac{1}{4}} - \frac{1}{2}\right]^2\right\}.$$

Using the relation for the steel–concrete mixture at the shock-wave front:

$$D = v_{s0}\sqrt{\frac{p}{v_{s0} - v(p)}}, \quad u = \sqrt{p(v_{s0} - v(p))}$$

we can construct the dependence of the shock-wave velocity on the mass velocity and determine the coefficients c_0 and q.

The failure of reinforced concrete is modeled with allowance for two failure mechanisms, namely, breaking and shear failures [4]. The local criterion for breaking failure is the ultimate value of the relative void volume ξ^*. When this criterion holds, a material is considered to be destroyed by breaking. The local criterion of shear failure is the ultimate value of the plastic-deformation intensity

$$e_u = \frac{\sqrt{2}}{3}\sqrt{3T_2 - T_1^2},$$

where $T_1 = \varepsilon_{ij}\delta_{ij}$ and $T_2 = \varepsilon_{ij}\varepsilon^{ij}$ are the first and second invariants of the strain tensor. When this value is attained, the material is considered to be destroyed according to the shear mechanism. In this case, cracks appear in the material, and opening of the cracks occurs under the action of tensile stresses. The behavior of the destroyed material is similar to that of a medium resisting compressive and shear forces but failed under the action of tensile forces.

The behavior of a solid explosive under a shock is also described in the framework of the model of a porous elastoplastic medium with an equation of state in the form of Eq. (1). The detonation arising under a certain condition is considered to occur instantaneously in the entire bulk of the material. The empirical equa-

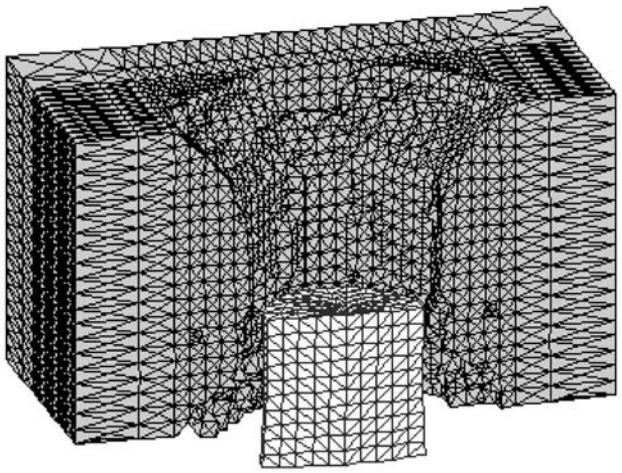

Fig. 2. Piercing of a concrete plate.

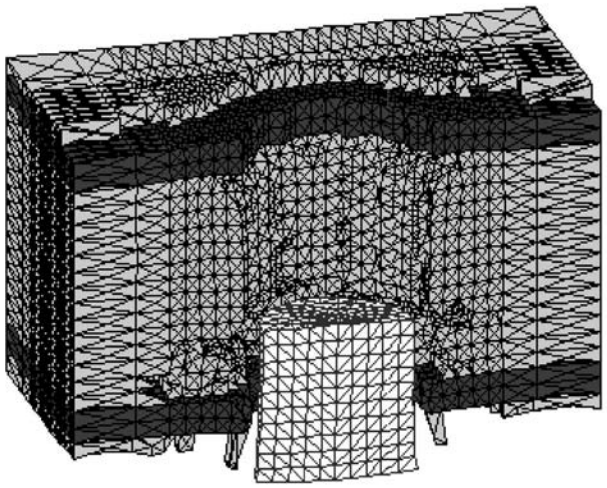

Fig. 3. Piercing of a reinforced-concrete plate.

tion of state (see [5]) is used for calculating the expansion of explosion products:

$$p = A\rho^n + \gamma\rho\varepsilon,$$

where $\gamma = \gamma_0 - c\rho$ and $c = \dfrac{\gamma_H - \gamma_0}{\rho_H}$ are the variable Grüneisen coefficient and volume sound velocity, respectively. A, n, ρ_H, γ_0, and γ_H are material constants.

For the given mathematical model, we now study an effect of the reinforcement of concrete on the piercing and failure of a reinforced-concrete plate by a compact steel striker. A reinforced-concrete plate is modeled by a structure consisting of concrete and reinforced concrete. Reinforcing the plate is performed by two fabrics with cells of 120 × 120 mm and steel bars 32 mm in diameter, which are immersed in concrete at a depth of 30 mm (Fig. 1). The striker is a steel cylinder with parameters $h = d_0 = 300$ mm. The results of a collision of the striker with a monolithic concrete plate are also given for comparison. The thickness of concrete and reinforced-concrete plates is $2d_0$; the shock speed is 300 m s^{-1}.

Table

Time, ms	$\frac{H}{d_0}$		u, m s^{-1}	
	concrete plate	reinforced-concrete plate	concrete plate	reinforced-concrete plate
0.2	0.17	0.17	254	246
0.5	0.42	0.39	240	214
1.8	1.25	1.16	151	141
3.5	1.98	1.84	119	89
4.3	2.3		116	
4.5		2.14		85
5.2		2.34		84

In the form of isomeric projections in the symmetry plane, Figs. 2 and 3 illustrate piercing of the reinforced-concrete plate at, respectively, 4.3 and 5.2 ms after the shock. The relative penetration depth $\dfrac{H}{d_0}$ of the striker and its velocity u as functions of time are shown in the table.

Piercing of the reinforced-concrete plate occurs 9 ms later as compared to the concrete plate, and the shock velocity is lower by 27.6% than in the latter case. The character of plate failure also differs significantly.

During the piercing of the concrete plate, breaking failure begins at 1.8 ms. The level of compressive stresses in the plate is 0.1 GPa < p < 0.26 GPa, the maximum values being attained in the region of the striker contact. Up to the very instant of piercing, a crater is being produced in the plate. The shape of the crater resembles two truncated cones with a common base $1.9d_0$ in diameter. The diameters of the upper and lower bases are $2.2d_0$ and $2.1d_0$, respectively.

Up to 1.8 ms, the striker pierces the first reinforced layer (in Fig. 4, concrete layer with a reinforcing fabric is shown as dark). In this case, the plate is subjected to the action of compressing stresses 0.05 GPa < p < 0.19 GPa. At 3.5 ms, the striker attains the second reinforced layer. Its piercing occurs at 4.5 ms. In consequence of the breaking failure, concrete flakes appear on the external side of the reinforced layers. Through holes $1.2d_0$ in diameter arise in the reinforced layers. Above the second reinforced layer inside the plate, fail-

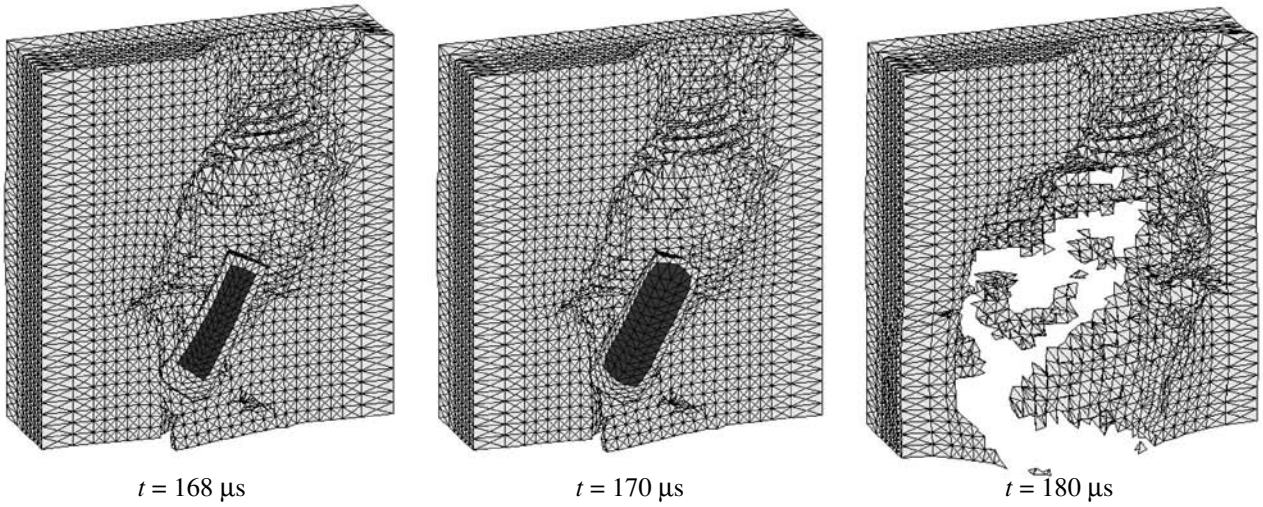

Fig. 4. Striker penetration into an obstacle composed of concrete–sand–concrete layers, which is accompanied by explosion of the striker.

ure occurs. The crater in the plate has a nearly cylindrical shape $1.2d_0$ in diameter.

Further, we analyze the penetration of a steel cylindrical striker into an obstacle composed of concrete–sand–concrete layers. Inside the striker, an explosive charge is introduced. The striker diameter is d_0 = 7.6 mm, and its height is $h = 4d_0$. The obstacle consists of two layers of fine-grain concrete, a layer of dry sand being placed between them. The thickness of the layers is the same and attains $2.98d_0$. The shock velocity is 800 m s^{-1}; the angle of incidence is 20°.

The calculated streak picture of the striker penetration and explosion is shown in Fig. 4. Piercing of the first concrete layer takes place up to 50 μs. Up to this instant, the striker velocity is 459 m s^{-1}. The penetration of the striker through the sand layer is completed up to 104 μs, the striker velocity decreasing to 363 m s^{-1}. A noticeable deformation of the striker head part is observed. The detonation of the striker explosive occurs at 168 μs when the striker velocity is 191 m s^{-1}. The maximum pressure of explosion products attains 26 GPa. As a result of their expansion, swelling of the striker steel shell and its failure occur. (Due to visualization difficulties, striker fragments and explosion products are not reproduced in Fig. 4.) Further, at 180 μs, as a result of the interaction of destroyed-shell fragments and explosion products with the obstacle, failure of the concrete plates occurs. It becomes even stronger with time, since the maximum pressure of explosion products remains significant and attains 5 GPa.

ACKNOWLEDGMENTS

This work was supported by the Russian Foundation for Basic Research, project no. 04-01-00856.

REFERENCES

1. V. M. Fomin, A. I. Gulidov, G. A. Sapozhnikov, *et al.*, *High-Speed Interaction of Solids* (Sib. Otd. Ross. Akad. Nauk, Novosibirsk, 1999) [in Russian].
2. A. L. Isaev, in *III Khariton's Scientific Meetings, Proc. Intern. Conf.* (VNIIÉF, Sarov, 2002), p. 150.
3. S. A. Afanas'eva, N. N. Belov, and N. T. Yugov, Dokl. Akad. Nauk **387**, 624 (2002) [Dokl. Phys. **47**, 876 (2002)].
4. N. N. Belov, V. N. Demidov, L. V. Efremova, *et al.*, Izv. Vyssh. Uchebn. Zaved., Fiz. **35** (8), 5 (1992).
5. É. V. Lin, in *Chemical Physics of Combustion and Explosion Processes. XII Symposium on Combustion and Explosion* (Chernogolovka, 2000), Part 3 [in Russian].

Translated by G. Merzon

Doklady Physics, Vol. 50, No. 3, 2005, pp. 136–139. Translated from Doklady Akademii Nauk, Vol. 401, No. 3, 2005, pp. 333–336.

THEORETICAL PHYSICS

Limited Distributions in the Statistical Theory of Gas Disperse Systems

Yu. I. Yalamov and A. N. Golov

Presented by Academician R.F. Ganiev July 1, 2004

Received September 23, 2004

1. When analyzing certain physical phenomena in gas disperse media, it is necessary to take into account both the microstructure of a medium, which is a system of a large number of disperse particles and gas molecules, and the microstructure of an individual particle. In this case, statistical theory and the corresponding distribution functions must be applied. Known distributions with unlimited values of random variables provide certain mathematical conveniences, but they cannot be accepted *a priori* in all cases. Their application can lead not only to numerical errors but also to the loss of certain dependences, particularly in nonequilibrium states. The artificial truncation of integrals is incorrect when distributions remain in the same form. Thus, we arrive at the important problem of finding distributions with a limited spectrum of certain variables.

There is a wide range of such problems, including a relativistic problem concerning the velocity distribution of particles whose velocities are lower than the maximum velocity. Quantum statistic problems with the limit on energy are known. A model with an upper energy limit for particles exists for a classical system surrounded by a finite-height potential barrier. A similar problem arises when considering volatile aerosol particles. Similar problems also arise upon the separation of disperse particles with a certain limiting velocity, when volume is limited, as in the classical model of harmonic oscillators, etc. Therefore, the problem is of current interest.

To estimate its application significance, we consider the example of the escape of atoms from a volatile solid particle. The table presents the maximum velocity v_m of atoms of the solid (an atom escapes from the solid when $v > v_m$) according to estimates based on the sum of the heats of phase transitions and their mean thermal velocity $\langle v \rangle$ at temperatures near the melting temperature. It is seen that velocity-limit corrections can reach 10% even if they are of the second order in $\frac{\langle v \rangle}{v_m}$.

Moscow State Regional University, ul. Radio, Moscow, 105005 Russia

In the above examples, restrictions are due to different causes, but a general formulation of this problem is both desirable and possible. Below, we propose a method for finding limited distributions of a certain type and present results for some models.

2. Following Prigogine's proposal, we start with the Liouville–Gibbs equation and complement the standard requirements on its solution by the zero boundary condition at finite values of certain variables. We consider only the classical variant of the theory, because the quantization procedure for the Liouville–Gibbs equation is well developed [1]. Following the method reported in [2], we transform the Liouville–Gibbs equation to the form

$$L_t \eta = 0. \quad (1)$$

Here, L_t is the time-dependent Liouvillian and $\eta = -\ln F_N$, where F_N is the distribution function. We consider only Gibbs and quasi-Gibbs solutions. In this case, the standard transition from statistical description to thermodynamics can be used. Both equilibrium and nonequilibrium states can be considered in such a formulation. Integrals of the homogeneous Liouvillian satisfy Eq. (1). These integrals are generalizations of the invariants of motion according to Noether's theo-

Table

Element	v_m, m/s	$\langle v \rangle$, m/s	$\frac{\langle v \rangle}{v_m}$
Ag	1281	308	0.24
Al	2740	536	0.2
Ca	1650	483	0.29
Cu	1821	420	0.23
Fe	2060	519	0.25
Hg	450	99	0.22
Kr	292	107	0.37
Pb	768	155	0.2
Pt	1293	294	0.23
Sn	1255	189	0.15

1028-3358/05/5003-0136$26.00

rem and are reduced to these invariants for closed systems in the absence of dissipative forces and nonideal constraints. The function η is sought in the form

$$\eta = \sum_{i=1}^{s} \eta_i, \quad (2)$$

where η_i are the functionals of s mentioned integrals. The requirements of the invariance of solutions under transformations corresponding to the symmetry of the problem are taken into account. The assumption of the statistical independence of phase variables is used when the model allows.

3. The stationary problem with condition $v \le v_m$ limiting the velocity of particles is the simplest case. Molecules or macroparticles in vacuum can be such particles. Phenomena associated with the structure of particles, their interaction, and external fields are disregarded. Velocity may be limited due to special relativity or other causes. A volatile particle surrounded by a potential barrier with a height of E_m is an example. Momentum and kinetic energy are invariants of motion. The functions η_i are formed by their even dimensionless superposition in the form of converging geometrical series (dimension scale is v_m). In this case, function (2) satisfies Eq. (1), and the corresponding function F_N is that solution of the Liouville–Gibbs equation that satisfies the boundary conditions $F_N(v_i = v_m) = 0$. For an isotropic uniform system of N identical particles with mass m in volume V, we obtain

$$F_N = Z_N^{-1} \exp\left[-\sum_{i=1}^{3N} \frac{m v_i^2}{2\Theta}\left(1 - \frac{v_i^2}{v_m^2}\right)^{-1}\right]. \quad (3)$$

The partition function is expressed in terms of the Whittaker function $W_{\lambda,\mu}$, but it is reduced to the more convenient form

$$Z_N = \left\{gmv_m \exp\left(\frac{g}{2}\right)\left[K_1\left(\frac{g}{2}\right) - K_0\left(\frac{g}{2}\right)\right]\right\}^{3N} V^N. \quad (4)$$

Here, $E_m = \frac{m v_m^2}{2}$, $g = \frac{m v_m^2}{2\Theta}$, is a dimensionless parameter, Θ is the asymptotic modulus of the distribution for $E_m \longrightarrow \infty$, and $K_\lambda(x)$ are cylindrical functions of an imaginary argument. Single-particle distributions of a similar form are known in relativistic kinetic theory [3–6], but they have been obtained from special-relativity requirements without assuming the statistical independence of variables. In relativistic theory, $g = \frac{m_0 c^2}{\Theta}$, and this parameter is very large ($\sim 10^{10}$–10^{11}) for most atomic systems. Therefore, relativistic corrections for such systems are insignificant, while the effects associated with formula (3) can be considerable. Computer calculations show that the single-particle distribution following from Eq. (3) in the isotropic approximation for $g \ge 100$ is close to the Landau function [5] with an accuracy of small fractions of a percent in the region $\frac{v}{v_m} \le 0.5$. Relativistic modification of the Liouville–Gibbs equation is not necessary to obtain Eq. (3), and this expression is preserved if the velocity restriction is nonrelativistic. This is important for applications, in which relativistic effects are very small, but other restrictions may include $v_m \ll c$, and the corresponding effects may be manifested under ordinary conditions (see table).

Knowing function (3), we can determine statistical means. Knowing function (4), we can find the free energy Ψ and all thermodynamic functions of the system according to Gibbs. In particular, the internal energy and entropy have the form

$$U = 3NE_m\left[\frac{K_1\left(\frac{g}{2}\right)}{K_1\left(\frac{g}{2}\right) - K_0\left(\frac{g}{2}\right)} - 1 - \frac{1}{g}\right],$$

$$\frac{S}{k_B} = \ln Z_N + \left[\frac{K_1\left(\frac{g}{2}\right)}{K_1\left(\frac{g}{2}\right) - K_0\left(\frac{g}{2}\right)} - 1 - g\right].$$

The pressure and thermodynamic properties of the system can be determined by standard formulas. The limiting transition of function (3) to the Maxwell distribution is obvious. However, the latter distribution does not satisfy the imposed boundary conditions and does not carry information on the barrier parameters.

4. The system of harmonic oscillators with a maximum energy of E_m is analyzed similarly. This model is applicable to solid clusters. Oscillations are assumed to be small in this model, but unlimited distributions integrable in infinite limits are often used. Limited distributions eliminate this contradiction. Since the consequences of new boundary conditions are of primary interest, we accept the simplest model of independent oscillators with the same frequency ω. In the general case, random values of momentum and coordinate can be correlated due to the conservation of the total energy E_m of oscillatory motion in a given degree of freedom. The same method provides the formulas

$$F_N = Z_N^{-1} \exp\left[-\sum_{k=1}^{3N} g(1 - s_k^2)^{-1}\right], \quad (5)$$

$$Z_N = \left\{\frac{\pi[g\mathrm{Ei}(-g) + \exp(-g)]}{ab}\right\}^{3N}, \quad (6)$$

where

$$g = \frac{E_m}{\Theta}, \quad s_k^2 = a^2 p_k^2 + b^2 q_k^2, \quad a^2 = \frac{1}{2mE_m},$$

$$b^2 = \frac{m\omega^2}{2E_m}.$$

Function (5) is represented as a product of the momentum and coordinate distributions only in the limit $E_m \longrightarrow \infty$. The partial momentum and coordinate distributions are determined by integrating function (5) with respect to the respective conjugate variables and have the form

$$F_v\{q_i\} = Z_N^{-1}\exp\left(-\sum_{k=1}^{3N}\xi_k\right)$$
$$\times\prod_{k=1}^{3N}\{a^{-1}(2g)^{1/2}\xi_k^{1/2}[K_1(\xi_k) - K_0(\xi_k)]\},$$

$$F_v\{p_i\} = Z_N^{-1}\exp\left(-\sum_{k=1}^{3N}\zeta_k\right)$$
$$\times\prod_{k=1}^{3N}\{b^{-1}(2g)^{1/2}\zeta_k^{1/2}[K_1(\zeta_k) - K_0(\zeta_k)]\},$$

where

$$\xi_k = \frac{g}{2(1-b^2q_k^2)}, \quad \zeta_k = \frac{g}{2(1-a^2p_k^2)}.$$

Here, p_k and q_k are also limited by the maximum values. Distribution (5) satisfies the correspondence principle. For large E_m values, it is close to the canonical distribution vanishing for $E_m \longrightarrow \infty$, but it significantly differs from the latter distribution when $\frac{E_m}{\Theta}$ is not too large (strongly heated states). When p and q are statistically independent, the distribution is represented as a product of a function of form (3) by a similar coordinate function.

5. We consider a system of noninteracting particles freely expanding to vacuum from a small instantaneous source. It may be a molecular cloud around a volatile disperse particle or an expanding cloud of nonvolatile particles. For simplicity, we consider a distribution depending on one pair of phase variables p and q. The generalization for many statistically independent degrees of freedom is evident. The homogeneous Liouvillian for this model has the integrals $I_1 = p$ and $I_2 = q - \frac{pt}{m}$. The unlimited time-dependent solution of the Liouville–Gibbs equation that satisfies the standard requirements has the form [2]

$$F(p, q, t) = A\exp(-aup^2 + kpq - bq^2), \qquad (7)$$

where

$$u = 1 + \frac{ct}{am} + \frac{bt^2}{am^2}, \quad k = c + \frac{2bt}{m},$$

and a, b, and c are the nonnegative constants of the problem. However, for unlimited p and q values, particles have arbitrarily large velocities and coordinates at the initial time.

The distribution that vanishes at $p = p_m$ and is unlimited as a function of q is obtained similarly in the form

$$F(p, q, t)$$
$$= Z^{-1}\exp\left[-(aup^2 - kpq + bq^2)\left(1 - \frac{p^2}{p_m^2}\right)^{-1}\right]. \qquad (8)$$

Integration of distribution (8) with respect to q yields the momentum distribution

$$F(p) = A\sqrt{\pi\left(1 - \frac{p^2}{p_m^2}\right)}\exp\left[-awp^2\left(1 - \frac{p^2}{p_m^2}\right)^{-1}\right],$$

where $w = 1 - \frac{c^2}{4ab}$ and A is the normalization constant. The distribution limited in the p and q variables has the form

$$F = A\exp\left[-\frac{g}{1-H}\right], \qquad (9)$$

where

$$H = \frac{f}{g}, \quad f = aup^2 - kpq + bq^2,$$
$$g = f(p = p_m, q = q_m).$$

For $k = 0$,

$$A = \sqrt{abw}\{\pi g[g\mathrm{Ei}(-g) + \exp(-g)]\}^{-1}.$$

The partial distributions are found from Eq. (8) in the form

$$F(q) = A(aw)^{-1/2}g\lambda^{1/2}\exp\left(-\frac{\lambda}{2}\right)\left[K_1\left(\frac{\lambda}{2}\right) - K_0\left(\frac{\lambda}{2}\right)\right],$$

$$F(p) = A(b)^{-1/2}g\mu^{1/2}\exp\left(-\frac{\mu}{2}\right)\left[K_1\left(\frac{\mu}{2}\right) - K_0\left(\frac{\mu}{2}\right)\right],$$

where

$$\lambda = \frac{g}{1 - \frac{bq^2}{g}}, \quad \mu = \frac{g}{1 - \frac{awp^2}{g}}.$$

These distributions describe the spatially limited system of particles with limited velocities and eliminate the aforementioned physically inconsistent properties.

6. The above distributions belong to a new class of solutions of the Liouville–Gibbs equation that satisfy the boundary conditions at finite phase variables and are obtained using a unified method. They enable one to eliminate certain contradictions that arise when solving a number of problems, satisfy the correspondence principle, and can be used in kinetic theory and statistical thermodynamics. The results show that the approach proposed above is fruitful when applied to the statistical theory of gas disperse systems and allows the inclusion of the characteristic features of a certain class of such systems.

When calculating integrals and dealing with special functions, we used handbooks [7, 8] and the Maple-8 package.

REFERENCES

1. I. Prigogine, *Non-Equilibrium Statistical Mechanics* (Interscience, New York, 1962; Mir, Moscow, 1964).
2. Yu. I. Yalamov and A. N. Golov, *Statistical and Mechanical Methods in the Theory of Nonequilibrium Molecular and Disperse Systems*, Available from VINITI, No. 2423-V92 (Moscow, 1992).
3. F. Juttner, Ann. Phys. Chem. **34**, 856 (1911).
4. D. van Dantzig, Proc. K. Ned. Akad. Wet. **42**, 608 (1939).
5. L. D. Landau and E. M. Lifshitz, *Statistical Physics* (Nauka, Moscow, 1976; Pergamon, Oxford, 1980).
6. S. R. de Groot, W. A. van Leeuwen, and Ch. G. van Weert, *Relativistic Kinetic Theory: Principles and Applications* (Elsevier, Amsterdam, 1980; Mir, Moscow, 1983).
7. E. Jahnke, F. Emde, and F. Losch, *Tables of Higher Functions* (McGraw-Hill, New York, 1960; Nauka, Moscow, 1977).
8. I. S. Gradshteyn and I. M. Ryzhik, *Table of Integrals, Series, and Products* (Nauka, Moscow, 1971; Academic, New York, 1980).

Translated by R. Tyapaev

Doklady Physics, Vol. 50, No. 3, 2005, pp. 140–142. Translated from Doklady Akademii Nauk, Vol. 401, No. 1, 2005, pp. 34–36.

MECHANICS

First Integrals in the Problem of the Motion of a Heavy Rigid Body Suspended on a String

A. A. Burov

Presented by Academician V.V. Rumyantsev July 5, 2004

Received July 15, 2004

The problem of the motion of a heavy rigid body suspended on an inextensible string is considered. The conditions ensuring the existence of first integrals, which hold both when the string is stretched and during free flight, are formulated. The possibility of extending the results to the case where the motion is executed by a chain of bodies is discussed.

It is known that three additional integrals are lacking for the integrability of the equations of the motion of a heavy body on a stretched string in the general case. However, this problem is completely integrable when the body is suspended at the center of mass. In this case, the integration is performed by separation of variables [1]. It is also known that the problem has one additional integral when the body is suspended at a point in the axis of dynamic symmetry [1]. The existence of particular integrals such as the Hess integral [2] for this problem was studied in [3]. The problem was generalized to the case of chains of rigid bodies in [4].

The general issue of the existence of first integrals in the problems of rigid-body dynamics in the presence of unilateral constraints was discussed in [5, 6].

FORMULATION OF THE PROBLEM AND EQUATIONS OF FREE MOTION

We will consider the motion of a heavy rigid body suspended at a fixed point $\mathcal{P}$ on an inextensible string. We will assume that the other end of the string is fixed at a point $\mathcal{Q}$ belonging to the body. Let $\mathcal{P}X_\alpha X_\beta X_\gamma$ be an absolute coordinate system (ACS) with the horizontal $\mathcal{P}X_\alpha$ and $\mathcal{P}X_\beta$ axes and the upward-directed vertical $\mathcal{P}X_\gamma$ axis. We will denote a movable coordinate system (MCS) fixed to the body by $\mathcal{C}x_1x_2x_3$. The origin of this system is at the center of mass $\mathcal{C}$ of the body, and its axes coincide with the principal central axes of inertia.

Since the string is assumed to be weightless, the motion of the center of mass of the body and the motion of the body about the center of mass can be separated for a time interval between impacts. The center of mass of the body moves along a parabola or a straight line, while the body itself rotates as an Euler gyroscope.

Let $\mathbf{X} = (X_\alpha, X_\beta, X_\gamma)$ be the vector $\overrightarrow{\mathcal{P}\mathcal{C}}$ projections onto the ACS axes and $\mathbf{V} = (V_\alpha, V_\beta, V_\gamma)$ be the center-of-mass velocity in the projections onto the same axes. We denote the center-of-mass and angular velocities in the projections onto the MCS axes by $\mathbf{v} = (v_1, v_2, v_3)$ and $\boldsymbol{\omega} = (\omega_1, \omega_2, \omega_3)$, respectively, and the vectors $\overrightarrow{\mathcal{P}\mathcal{C}}$, $\overrightarrow{\mathcal{P}\mathcal{Q}}$, $\overrightarrow{\mathcal{C}\mathcal{Q}}$ and the unit vector of the upward vertical in the projections onto the same axes by $\mathbf{x} = (x_1, x_2, x_3)$, $\boldsymbol{\ell} = (\ell_1, \ell_2, \ell_3)$, $\mathbf{c} = (c_1, c_2, c_3)$, and $\boldsymbol{\gamma} = (\gamma_1, \gamma_2, \gamma_3)$, respectively. Now, if m is the body mass, $\mathbf{I} = \mathrm{diag}(I_1, I_2, I_3)$ is its principal central inertia matrix, and g is the gravitational acceleration, then the kinetic energy of the body and the potential energy of the system are represented in the form

$$T = (T_V + T_\omega)$$

$$= \frac{1}{2}m\mathbf{V}^2 + \frac{1}{2}(\mathbf{I}\boldsymbol{\omega}, \boldsymbol{\omega}) = \frac{1}{2}m\mathbf{v}^2 + \frac{1}{2}(\mathbf{I}\boldsymbol{\omega}, \boldsymbol{\omega}),$$

$$U = mgX_\gamma.$$

The rotational motion of the body during free flight can conveniently be described by the equations

$$\dot{\mathbf{I}\boldsymbol{\omega}} = \mathbf{I}\boldsymbol{\omega} \times \boldsymbol{\omega}, \quad \dot{\boldsymbol{\gamma}} = \boldsymbol{\gamma} \times \boldsymbol{\omega}. \tag{1}$$

The motion of the center of mass can be described by either the ACS equations

$$\dot{V}_\alpha = 0, \quad \dot{V}_\beta = 0, \quad \dot{V}_\gamma = -g, \quad \dot{\mathbf{X}} = \mathbf{V}, \tag{2}$$

or the MCS equations

$$\dot{\mathbf{v}} = \mathbf{v} \times \boldsymbol{\omega} - g\boldsymbol{\gamma}, \quad \dot{\mathbf{x}} = \mathbf{v} + \mathbf{x} \times \boldsymbol{\omega}. \tag{3}$$

In this case, the translational and rotational motions of the body are completely separated, and the equations themselves are completely integrable. The integrals

$$\mathcal{J}_\omega = T_\omega, \quad \mathcal{J}_V = T_V + U$$

Dorodnitsyn Computer Center,
Russian Academy of Sciences,
ul. Vavilova 40, GSP-1, Moscow, 117333 Russia

1028-3358/05/5003-0140$26.00

express the conservation of the kinetic energy of rotation and the total energy of translation.

Moreover, the projection of the total kinetic moment onto the vertical $\mathcal{J}_\psi = (\mathbf{I}\boldsymbol{\omega} + m\mathbf{x} \times \mathbf{v}, \boldsymbol{\gamma})$ is also conserved during free motion. Finally, the integral $\mathcal{J}_\gamma = (\boldsymbol{\gamma}, \boldsymbol{\gamma}) - 1 = 0$ represents the fact that $\boldsymbol{\gamma}$ is a unit vector.

TRANSFORMATION OF VELOCITIES FOR THE CASE OF THE STRETCHED STRING

We will now assume that the string is stretched at a certain time. Then, the position of the body is unchanged at the moment of interaction, while the center-of-mass and angular velocities are transformed in accordance with a rule $(\mathbf{V}, \boldsymbol{\omega}) \longrightarrow (\mathbf{V}', \boldsymbol{\omega}')$ determined by the equations

$$\mathbf{I}(\boldsymbol{\omega}' - \boldsymbol{\omega}) = \mathbf{c} \times (-R\ell), \quad m(\mathbf{v}' - \mathbf{v}) = -R\ell. \tag{4}$$

Statement 1. *The scalar quantities*

$$\mathcal{J}_c = (\mathbf{I}\boldsymbol{\omega}, \mathbf{c}), \quad \mathcal{J}_\ell = (\mathbf{I}\boldsymbol{\omega}, \ell) \tag{5}$$

and the vector quantities

$$\mathcal{J}_1 = \mathbf{I}\boldsymbol{\omega} + m\mathbf{c} \times \mathbf{v}, \quad \mathcal{J}_2 = \ell \times \mathbf{v} \tag{6}$$

are conserved during the impact.

The proof of relations (5) reduces to the scalar multiplication of the left and right-hand sides of the first of Eqs. (4) by the vectors ℓ and $\mathbf{c}$, respectively. To prove the first of Eqs. (6), we perform the vector multiplication of the left and right-hand sides of the second of Eqs. (4) by the vector $-\mathbf{c}$ from the left and add the result to the first of Eqs. (4). To prove the second of relations (6), it is sufficient to perform the vector multiplication of the second of Eqs. (4) by ℓ from the left.

Note. Combining the integrals $\mathcal{J}_1$ and $\mathcal{J}_2$, we can ascertain that the quantity $\mathcal{J}_\psi$ is also conserved during the impact. Moreover, this note is valid according to the general theory of the symmetries of mechanical systems subject to unilateral constraints (see, e.g., [7]).

DETERMINATION OF REACTIONS

For definiteness, we will assume that the impact occurs without loss of energy. Since the potential energy of the system depends only on the body position that does not change at the impact moment, to determine the quantity R we will use the kinetic-energy-conservation condition

$$(\mathbf{I}\boldsymbol{\omega}', \boldsymbol{\omega}') + m\mathbf{v}'^2 = (\mathbf{I}\boldsymbol{\omega}, \boldsymbol{\omega}) + m\mathbf{v}^2. \tag{7}$$

We perform the scalar multiplication of the first and the second of Eqs. (4) by $\boldsymbol{\omega}' + \boldsymbol{\omega}$ and $\mathbf{v}' + \mathbf{v}$, respectively. Summing the results, by virtue of Eq. (7), we arrive at the result

$$\begin{aligned}&(\mathbf{I}\boldsymbol{\omega}', \boldsymbol{\omega}') + m\mathbf{v}'^2 - (\mathbf{I}\boldsymbol{\omega}, \boldsymbol{\omega}) - m\mathbf{v}^2 \\ &= R[(\boldsymbol{\omega}' + \boldsymbol{\omega}, \mathbf{c} \times (-\ell)) + (\mathbf{v}' + \mathbf{v}, (-\ell))] = 0.\end{aligned} \tag{8}$$

Expressing $\boldsymbol{\omega}'$ and $\mathbf{v}'$ from Eqs. (4), we obtain

$$\boldsymbol{\omega}' = \boldsymbol{\omega} - R \cdot \mathbf{I}^{-1}(\mathbf{c} \times \ell), \quad \mathbf{v}' = \mathbf{v} - m^{-1}R\ell. \tag{9}$$

Substituting relations (9) into Eq. (8), we find that the nonzero root of Eq. (7) is determined from the equation

$$\begin{aligned}&(2\boldsymbol{\omega} + R \cdot (\mathbf{I}^{-1}(\mathbf{c} \times (-\ell)), \mathbf{c} \times (-\ell))) \\ &+ (2\mathbf{v} - m^{-1}R\ell, (-\ell)) = 0\end{aligned}$$

in the form

$$R = 2\frac{(\mathbf{v}, \ell) + (\boldsymbol{\omega}, \mathbf{c} \times \ell)}{m^{-1}\ell^2 + (\mathbf{I}^{-1}(\mathbf{c} \times \ell), \mathbf{c} \times \ell)}. \tag{10}$$

THE CASE OF DYNAMIC SYMMETRY

We will assume that the body is dynamically symmetric with an axis of symmetry, for example, $\mathcal{C}x_3$ and that the suspension point $\mathcal{Q}$ belongs to this axis. Then, we have

$$I_1 = I_2, \quad c_1 = c_2 = 0, \tag{11}$$

and, by virtue of Eq. (4), the following equality holds:

$$\omega_3' = \omega_3.$$

Thus, this integral, which holds in the absence of an unilateral constraint, is also valid when the constraint is imposed.

ANALOG OF THE HESS–APPELROT CASE

Let $I_1 > I_2 > I_3$ for definiteness. It is known that, if

$$\mathbf{a} = (a_1, a_2, a_3):$$

$$a_1 = \sqrt{I_2^{-1} - I_1^{-1}}, \quad a_2 = 0, \quad a_3 = \sqrt{I_3^{-1} - I_2^{-1}},$$

then the case of free motion has particular integrals, or invariant relations

$$\mathcal{F}_\varepsilon = a_1 I_1 \omega_1 + \varepsilon a_3 I_3 \omega_3 = 0, \quad \varepsilon = \pm 1. \tag{12}$$

Statement 2. *If the conditions*

$$a_1 c_3 - \varepsilon a_3 c_1 = 0, \quad c_2 = 0, \tag{13}$$

are fulfilled, then particular integrals (12) *are valid not only for the motion of a body with a stretched constraint but also for the motion with impacts.*

Note 1. If the body is suspended on several strings and all the suspension points satisfy relations (13), then the statement is also valid, at least for motions with nonmultiple impacts.

Note 2. The statement is also valid if the body is suspended on extensible weightless strings whose suspension points satisfy relations (13).

EXTENSION OF THE RESULTS TO THE CASE OF A HEAVY GYROSTAT

Under certain conditions, the results concerning the existence of the integrals of the equations of motion of a heavy rigid body suspended on a string can be extended to a heavy gyrostat.

In the case of the stretched string, the motion can be described by the equations

$$\mathbf{I}\dot{\boldsymbol{\omega}} = (\mathbf{I}\boldsymbol{\omega} + \mathbf{k}) \times \boldsymbol{\omega} + \mathbf{c} \times (-R\ell), \quad \dot{\boldsymbol{\gamma}} = \boldsymbol{\gamma} \times \boldsymbol{\omega}, \quad (14)$$

where $\mathbf{k} = (k_1, k_2, k_3)$ is the gyrostatic moment vector, which is constant throughout the body, and R is the constraint reaction determined from the condition that the string is inextensible.

Statement 3. *If the dynamic symmetry conditions given by Eqs.* (11) *are fulfilled, together with the condition* $\mathbf{k} = (0, 0, k_3)$*, then Eqs.* (14) *admit the integral* $\mathcal{J}_3 = \omega_3$.

If conditions (13) are fulfilled, together with the conditions

$$k_2 = 0, \quad \delta I_2 a_1 a_3 = a_3 k_1 - \varepsilon a_1 k_3,$$

then there is the particular integral

$$\mathcal{F}_\varepsilon = a_1 I_1 \omega_1 + \varepsilon a_3 I_3 \omega_3 + \delta = 0, \quad (15)$$

which is analogous to the Sretenskiĭ integral [7].

The same integrals exist for the motion of the heavy gyrostat with impacts, as well as for the case of an extensible string.

ACKNOWLEDGMENTS

This work was supported by the Russian Foundation for Basic Research, project no. 02-01-00196, and the Federal Program “Integratsiya.”

REFERENCES

1. V. V. Rumyantsev, Izv. Akad. Nauk SSSR, Mekh. Tverd. Tela, No. 4, 5 (1983).
2. W. Hess, Math. Ann. **37** (2), 153 (1895).
3. A. A. Burov, Izv. Akad. Nauk SSSR, Mekh. Tverd. Tela, No. 2, 84 (1987).
4. V. N. Rubanovskiĭ and G. V. Gorr, Prikl. Mat. Mekh. **52**, 707 (1988).
5. T. V. Kozlova, Vestn. Mosk. Univ., Ser. 1: Mat., Mekh., No. 3, 69 (2001).
6. T. V. Kozlova, J. Phys. A: Math. Gen. **34** (11), 2121 (2001).
7. S. N. Berezinskaya, O. V. Sorokina, and E. I. Kugushev, Preprint No. 16, IPM (Inst. of Applied Mathematics, Russian Academy of Sciences, 2003).
8. L. N. Sretenskiĭ, Vestn. Mosk. Univ, Ser. 1: Mat., Mekh., No. 3, 60 (1963).

Translated by M. Lebedev

Doklady Physics, Vol. 50, No. 3, 2005, pp. 143–146. Translated from Doklady Akademii Nauk, Vol. 401, No. 1, 2005, pp. 37–40.

MECHANICS

Shaping a Nozzle with a Central Body by the Chaplygin Method

É. G. Shifrin and Ch. V. Kim

Presented by Academician O.M. Belotserkovskiĭ June 25, 2004

Received July 14, 2004

We calculate the coordinates of an axisymmetric nozzle with a central body. This nozzle ensures a transonic flow with a plane sound surface, which is orthogonal to the symmetry axis and has a wall kink at the sonic point. A modification of the numerical method previously developed in [1–4] for shaping plane and axisymmetric De Laval nozzles is applied. As in [1–4], the Chaplygin transformation in the subsonic part of the flow leads to the Dirichlet problem for a system of nonlinear equations. The definition domain of the solution in the velocity-hodograph plane is taken as a rectangle similar to [1–4]. This enables one to obtain the nozzle with a monotonic distribution of velocity along its subsonic part. In the nonlinear differential equation, the linear Chaplygin operator for plane flows is separated, which allows the iterative calculation of the solution. The supersonic part of the nozzle is calculated under the assumption that the flow at the nozzle exit is uniform and parallel to the symmetry axis; i.e., the supersonic jet outflows to the submerged space with the same pressure. The calculation is performed by the characteristic method. The exact solution [2] for near-sonic flows with the straight sonic line is used to "move away" the sound plane. The velocity distribution along the supersonic part of the nozzle is also monotonic, which ensures the absence of the boundary-layer separation and, therefore, the adequacy of the ideal-gas model. Calculations show that the flow in the supersonic part of the nozzle is continuous (compression shocks are absent).

A ring (axisymmetric) De Laval nozzle with a "central body" is of great engineering interest [5, 6]. We determine the contour of such a nozzle with the following properties.

(i) The transition through the speed of sound occurs on a plane sound surface orthogonal to the symmetry axis.

Institute of Design Automation,
Russian Academy of Sciences, Moscow, Russia
e-mail: shifrin@icad.org.ru

(ii) The flow velocity does not decrease along the entire contour. This property ensures the adequacy of the ideal-gas model (with boundary-layer corrections) for any Reynolds numbers. Therefore, the flow separation regions and corresponding energy losses are absent.

(iii) The nozzle-contour kink at the sonic point makes it possible to obtain the nozzle of the minimum length. In this case, as was proved in [7], the flow near the corner point is not decelerated. In addition, there is no compression shock emerging from the corner point when it is placed on the curvilinear sound surface.

The gas dynamic equations for axisymmetric potential flows were transformed to the variables τ and β in [1, 2, 4]. The right-hand side of the nonlinear (in contrast to the plane case) Chaplygin equation includes the Jacobian J of mapping into the hodograph plane and the physical-plane ordinate $y(\tau, \beta)$, which is described by the solution of the Cauchy problem for the ordinary differential equation

$$\begin{aligned}
&2\tau\psi_{\tau\tau} + (3 - 2\tau R)\psi_\tau + R\psi_{\beta\beta} \\
&\quad = -Q(2J\cos\beta + J_\beta \sin\beta), \\
&J = -\frac{2\tau(\psi_\tau)^2 + R(\psi_\beta)^2}{Q(\psi_\beta \sin\beta + y^2 Q)}, \\
&R = \frac{\tau^* - \tau}{2\tau^*\tau(1-\tau)}, \qquad (1) \\
&Q = \sqrt{\frac{\tau}{\tau^*}}(1-\tau)^{1/(k-1)}, \\
&\forall \tau \in \left[0, \frac{k-1}{k+1}\right], \\
&\frac{\partial y(\tau, \beta)}{\partial \beta} = \frac{2\tau\sin\beta\psi_\tau - \cos\beta\psi_\beta}{yQ}.
\end{aligned}$$

Here, $\tau = \dfrac{|V|}{|V|_{\max}}$ is the Chaplygin variable, β is the velocity argument, $\psi(\tau, \beta)$ is the stream function, and k is the adiabatic index.

1028-3358/05/5003-0143$26.00

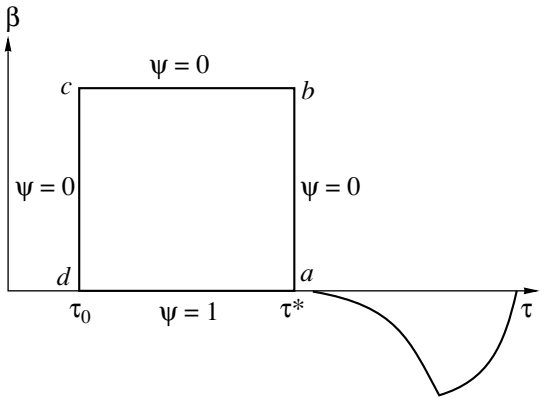

Fig. 1. Flow definition domain in the (τ, β) plane.

We solve the problem of shaping the nozzle in the class of flows with the plane sound surface. In the potential axisymmetric flow, such a surface is necessarily orthogonal to the symmetry axis [8]. This property enables one to design the subsonic and supersonic parts of the nozzle independently. Moreover, the contour kink can be introduced at the sonic point in the supersonic region.

Subsonic part of the nozzle. The image of the subsonic-flow region in the (τ, β) plane is specified in the form of a rectangle $D = abcd$, where ab is the segment of the sonic line $\tau = \frac{k-1}{k+1}$, ad and bc are the segments of the straight lines $\beta = 0$ and $\beta = \beta_0$, respectively; and dc is the segment of the straight line $0 \le \tau = \tau_0 < \frac{k-1}{k+1}$ (Fig. 1). The piecewise continuous boundary condition $\psi = 1$ on ad and $\psi = 0$ on ab, bc, and cd is specified at the boundary of D. In addition, $y = \text{const}$ is specified on ad. These conditions determine the Dirichlet problem for system (1).

By analogy with a plane flow, one can assume that the solution of this problem $\psi(\tau, \beta) \in C^2(D)$ finite in $\bar{D}$ exists and satisfies the boundary condition at its continuity points. In view of the one-to-one nature of the mapping of D onto the subsonic-flow region in the physical plane, this solution has the following properties.

(i) The velocity distribution along the nozzle wall (in the direction from the nozzle entrance) is a nondecreasing function of the arc length.

(ii) The one-to-one nature of the mapping breaks down at the points a and d, where the stream function ψ has the first-kind discontinuities. The point a presents the segment of the straight sonic line (its length is determined by the gas rate through the nozzle that correspond to the unit discontinuity of the stream function). The point d presents the entry nozzle section that is at infinity from the sonic line.

(iii) One wall of the nozzle is a circular cylinder parallel to the symmetry axis, which is the image of the segment ad. The other wall consists of two curvilinear sections (the images of segments ab and cd, on which velocity is constant) smoothly matched with each other by the straight (conic) section bc, where the velocity increases monotonically from the entry value corresponding to τ_0 to the speed of sound.

As in [1–4], we use the approximating algebraic system obtained by changing derivatives in the differential equation to the central finite-difference formulas of the second order of accuracy. This system is solved by the iterative method with sequential sweeps at each iteration along the inner straight lines $\tau_i = \text{const}$, $i = 1, 2, \ldots, I$. After the "practical convergence" of the iterative process, the nozzle coordinates are obtained by integrating the expressions for the derivatives

$$x_\tau = -\frac{R\psi_\beta \cos\beta + JQ\sin\beta\cos\beta + \psi_\tau \sin\beta}{yQ},$$

$$x_\beta = \frac{\psi_\tau \cos\beta + JQ\sin^2\beta + R\psi_\beta \sin\beta}{yQ},$$

$$y_\tau = \frac{2\cos\beta\psi_\tau - \sin\beta\psi_\beta}{yQ},$$

$$y_\beta = \frac{2\tau\sin\beta\psi_\tau - \cos\beta\psi_\beta}{yQ}$$

along three sides of the rectangle $abcd$. The derivatives normal to the boundary are calculated by three-point finite difference formulas of the second order of accuracy.

As in [4], to avoid the instability of the iterative process, the mixed derivative $\psi_{\tau\beta}$ is approximated on a seven-point template, which does not include points a and d (where ψ is discontinuous) at the appropriate orientation of the template. We emphasize that the iterations converge much more slowly than in the plane case.

Figure 3 shows the results of the calculations for various nozzle contours.

Supersonic part of the nozzle. The supersonic-flow region consists of two subregions. In the first subregion adjacent to the straight sonic line, the flow turning at the corner point of the contour is accelerated. This subregion is bounded by the sonic line AA', the last characteristic AD of the rarefaction node (Prandtl–Mayer flow) and cylinder wall $A'D$ parallel to the symmetry axis. The second subregion is bounded by the shaped supersonic section AE of the nozzle contour, the characteristic AD, and the straight-line characteristic DE passing from the end point of the shaped contour section to the outer cylinder wall (Fig. 2). At the characteristic DE, the supersonic flow is uniform and parallel to

the symmetry axis. When the pressure in the submerged space coincides with the pressure at the jet boundary downstream of the characteristic *DE*, the flow in the jet remains uniform and straight. When the pressure in the jet is higher than the pressure in the submerged space (underexpanded jet), the flow expands downstream of the characteristic *DE*, turning around the point *D*. When the pressure in the jet is lower than the pressure in the submerged space (overexpanded jet), compression shocks generally arise upstream of the characteristic *DE*. In this case, the Mach reflection from the central body, as well as the separation of the flow from the cylinder wall *A'D* of the nozzle, is possible. The flow in the underexpanded jet was not calculated. This calculation should be performed separately with a modified algorithm.

The supersonic part of the contour is calculated in several stages.

(i) The characteristic of the first family *A"A"'* is calculated near the sonic line. This enables us to avoid the degeneration of the characteristic method by moving away the straight sonic line.

(ii) The characteristic of the second family *A"B* in the Prandtl–Mayer flow is calculated near the corner point.

(iii) The solution is calculated in the domain *A"'A"BD* (between two characteristics obtained at the first two stages). At this stage, the solution is calculated first in the characteristic quadrilateral *A"'A"BC* and then in the triangle *A"'CD* bounded by the cylinder wall.

(iv) The contour of the central body, section *AE*, is calculated.

The characteristic *A"A"'* is determined with the use of the exact solution of the Tricomi equation [1, 2, 4] that describes the plane near-sonic flow near the straight sonic line, which arises due to the symmetric interaction between two centered rarefaction waves (i.e., due to the reflection of the Prandtl–Mayer flow from the symmetry axis).

This exact solution is given by the improper integral

$$\Psi = C_1 \int_{+\infty}^{z} \frac{dz}{\left(z^3 - \frac{9}{4}\right)^{5/6}} + C_2, \quad z \in \left[\left(\frac{9}{4}\right)^{1/3}, \infty\right].$$

We calculate this solution by dividing the integration region into three sections:

$$\left(\frac{9}{4}\right)^{1/3} \le z_1 < \left(\frac{9}{4}\right)^{1/3} + 0.0001,$$

$$\left(\frac{9}{4}\right)^{1/3} + 0.0001 \le z_2 < \left(\frac{9}{4}\right)^{1/3} + 0.1,$$

$$\left(\frac{9}{4}\right)^{1/3} + 0.1 \le z_3 \le \infty.$$

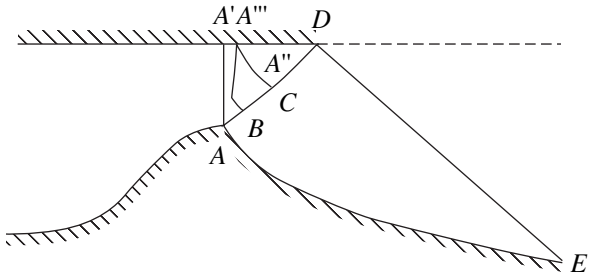

Fig. 2. Flow definition domain in the physical (*x*, *y*) plane.

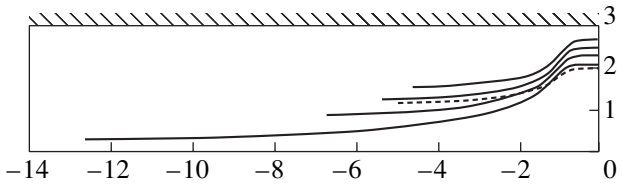

Fig. 3. Contours of the subsonic part of the nozzle for $\tau_0 = 0.01$. Different lines correspond to different sonic-line segments. The dashed line is the contour for $\tau_0 = 0.02$.

Asymptotic expressions are used in the first and third sections, and numerical methods, in the second section.

The use of this exact solution can be justified as follows. Since the radial velocity component in the straight sonic line, which is orthogonal to the symmetry axis, is equal to zero, the equations of the characteristics of the plane and axisymmetric flows on the straight sonic line coincide with each other. Therefore, if a characteristic (beginning at a point far from the symmetry axis) is close to the straight sonic line, it differs slightly from a characteristic of the same family in the plane flow.

Upon turning at the corner point by means of the Prandtl–Mayer flow, there are three possible cases. If the flow turns slightly, the supersonic part of the nozzle contour does not reach the symmetry axis; i.e., $\beta_E \neq 0$ and $y_E > 0$ at the point *E*. If the turn of the flow is too large, the central-body contour cannot be shaped by the characteristic method so that it can reach and touch the symmetry axis. Indeed, according to the Nikol'skiĭ theorem [9], there is no continuous axisymmetric supersonic flow near the thinning point of a body with a nonzero inner angle (the characteristic *DE* cannot reach the symmetry axis in the continuous velocity field so that $\beta_E \neq 0$ and $y_E = 0$). Therefore, the flow turning angle at the corner point of the contour must be chosen such that the equalities $\beta_E = 0$ and $y_E = 0$ are satisfied. Such a choice in the computational process is made by varying flow-turning values at the point *A*.

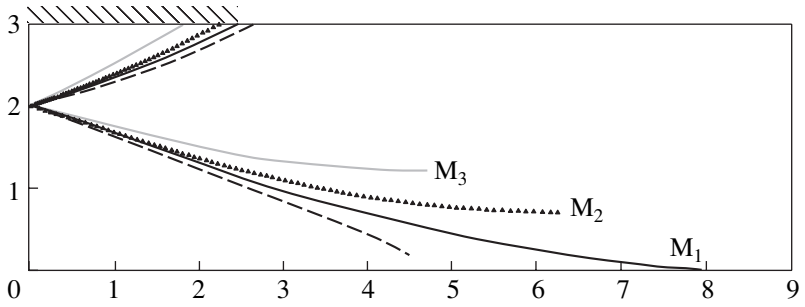

Fig. 4. Contours of the supersonic part of the nozzle for the exit Mach numbers $M_1 = 2.125$, $M_2 = 2.040$, and $M_3 = 1.881$. The dashed line is the contour corresponding to an excessively large flow turning at the point *A*.

The results of the calculations are shown in Fig. 4.

REFERENCES

1. E. G. Shifrin and O. M. Belotserkovskii, *Transonic Vortical Gas Flows* (Wiley, Chichester, 1994).
2. É. G. Shifrin, *Potential and Transonic Vortical Flows of an Ideal Gas* (Fizmatlit, Moscow, 2001) [in Russian].
3. N. A. Podsypanina and É. G. Shifrin, Izv. Akad. Nauk SSSR, Mekh. Zhidk. Gaza, No. 1, 54 (1975).
4. N. A. Podsypanina, Izv. Akad. Nauk SSSR, Mekh. Zhidk. Gaza, No. 1, 164 (1977).
5. J. J. Korte, A. O. Salas, H. J. Dunn, *et al.*, NASA Techn. Memorandum, No. 110326, 1 (1997).
6. T. Ito, K. Fujii, and A. K. Hayashi, AIAA Pap., No. 3211, 768 (1999).
7. É. G. Shifrin, Izv. Akad. Nauk SSSR, Mekh. Zhidk. Gaza, No. 1, 168 (1981).
8. É. G. Shifrin, Prikl. Mat. Mekh. **29** (4), 796 (1965).
9. A. A. Nikol'skiĭ, in *Collection of Theoretical Works on Aerohydrodynamics* (Oborongiz, Moscow, 1957), pp. 74–76 [in Russian].

Translated by R. Tyapaev

Doklady Physics, Vol. 50, No. 3, 2005, pp. 147–150. Translated from Doklady Akademii Nauk, Vol. 401, No. 2, 2005, pp. 189–192.

MECHANICS

Nonlinear Sinusoidal and Varicose Instability in a Boundary Layer

Yu. A. Litvinenko[1], V. G. Chernoraĭ[1], V. V. Kozlov[1], L. Lofdahl[2], G. R. Grek[1], and H. H. Chun[3]

Presented by Academician V.E. Nakoryakov October 7, 2004

Received October 15, 2004

It is well known [1] that the laminar–turbulent transition at a low turbulence level of the free flow is associated with the development of instability waves, the so-called Tollmien–Schlichting waves. When a two-dimensional Tollmien–Schlichting wave reaches a certain amplitude at the nonlinear stage of its development, it undergoes three-dimensional distortion and, as a result, characteristic three-dimensional Λ structures arise [1]. Owing to certain features of the appearance and development of these structures, they are not only typical for the classical laminar–turbulent transition, but are also inevitable attributes of a transition to more complex flows, e.g., flows modulated with longitudinal streaky structures, such as Hertler vortices, transverse-flow vortices on sliding wings, etc., as well as flows in the viscous sublayer of a turbulent boundary layer. In these cases, they arise in particular due to the secondary high-frequency instability of such flows and may be manifested not only as Λ structures, but also in the form of horseshoe vortices (Ω structures), hairpin vortices, etc. A characteristic feature of the development of such structures, e.g., on a sliding wing, is the disappearance of one of the counter-rotating vortices due to the transverse flow, whereas the development of a classical Λ structure can be observed on a straight wing [1].

The high-frequency secondary instability of transition and turbulent near-wall flows in the presence of streaky structures is often attributed to so-called sinusoidal and varicose instability. Both instability modes were investigated under controlled conditions at the linear and initial stages of nonlinear development. When the transverse size of the streaky structure was larger than the thickness of the shear layer, growth of varicose instability was observed. At the same time, when the transverse size of the streaky structure was comparable to or smaller than the thickness of the shear layer, it became more instable with respect to antisymmetric (sinusoidal) modes than to symmetric (varicose) modes. The experiment reported in [2] clearly shows that the growth of the symmetric mode leads to the formation of hairpin vortices, which are a pair of counter-rotating longitudinal vortices that are connected by a head, i.e., a Λ vortex, while an antisymmetric mode is developed to a train of quasi-longitudinal vortices with alternating-sign vorticity. Unfortunately, the experiments reported in [2] concerned only the initial stage of the nonlinear development of disturbances, and spatial resolution was insufficiently high to reveal the structure of the flow in more detail.

In this paper, we report on our experimental investigations of the nonlinear stage of the varicose and sinusoidal instability of the streaky structure in the Blasius boundary layer. In contrast to the experiment reported in [2], the study is more detailed (thermal anemometer measurements of the longitudinal velocity component and velocity pulsations in space (*xyz*) at 5×10^4 points) in order to reveal the features of the dynamics of the appearance, development, and internal structure of coherent formations up to the later stages of their nonlinear development.

The experiments were carried out under controlled conditions in a low-turbulent wind tunnel. A plane plate 14 mm in thickness, 1000 mm in width, and 2000 mm in length was placed in parallel in the operation part of the tunnel. The streaky structure was generated by means of a cylindrical roughness element, which had a height of 1.1 mm and a diameter of 5.8 mm and was placed in the center of the plate at a distance of x_0 = 438 mm from the fore. The velocity of the flow was equal to U_∞ = 7.8 m/s, and the turbulence level was no higher than 0.04%. In the absence of the roughness element, the laminar boundary layer was developed without any waves and the velocity profile was close to the Blasius profile. A roughness-element height of h = 1.1 mm is close to the thickness of the displacement of

[1] *Institute of Theoretical and Applied Mechanics, Siberian Division, Russian Academy of Sciences, ul. Institutskaya 4/1, Novosibirsk, 630090 Russia*
e-mail: kozlov@itam.nsc.ru

[2] *Charmers University of Technology, S-41296 Göteborg, Sweden*

[3] *Pusan National University, 609-735 Pusan, Korea*

1028-3358/05/5003-0147$26.00

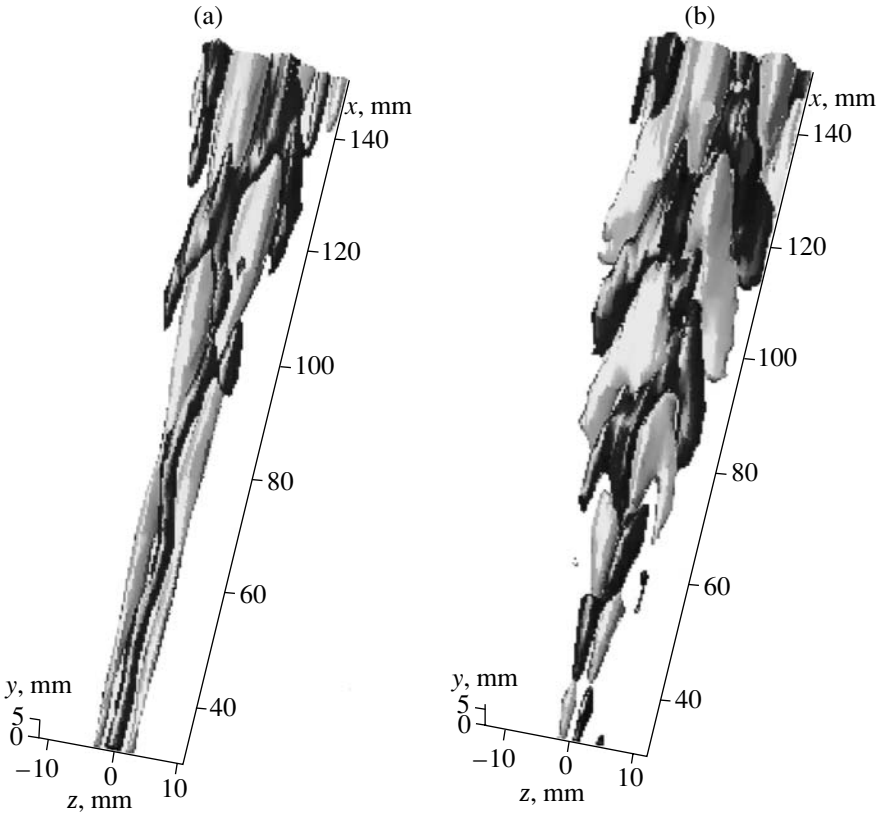

Fig. 1. Spatial patterns of the sinusoidal destruction of the streaky structure: (a) the development of the secondary disturbance jointly with its effect on average velocity (minimum pulsation level 6.4% of U_∞) and (b) the development of the secondary high-frequency disturbance (minimum pulsation level 1.3% of U_∞). Dark and light grey tones are excesses and defects of velocity, respectively.

the Blasius laminar boundary layer $\delta_B^* = 1.5$ mm for $x = x_0$ and $U_\infty = 7.8$ m/s. The Reynolds number was equal to $R^* = \frac{\delta_B^* U_\infty}{\nu} = 780$ for $x = x_0$. In the absence of artificial disturbances, the boundary layer with the streaky structure remained laminar in the measured range $x - x_0 = 30$–150 mm. This circumstance enabled us to control the instability of the streaky structure by means of artificial disturbances generated by the injection–drainage of a gas through three small holes on the plate surface. One hole ($z = 0$) at $x - x_0 = 14.5$ mm was used to excite transverse symmetric disturbances, and other two holes were used to excite antisymmetric disturbances $\Delta z = \pm 4.5$ mm at $x - x_0 = 19.5$ mm. The excited frequency of the secondary high-frequency disturbance was equal to 150 Hz, which approximately corresponded to a dimensionless parameter of $\frac{2\pi f \nu}{U_\infty^2} \times 10^6 = 232$. The amplitude of the secondary disturbance reached 10% of U_∞ near the source ($x - x_0 = 30$ mm), which made it possible to study the nonlinear stage of the process that was of primary interest. The thermal anemometer measured the time-averaged longitudinal component of the velocity U and velocity pulsation u'.

We consider the flow structure at the nonlinear stage of sinusoidal and varicose instability in more detail. Figure 1 shows patterns of the sinusoidal destruction of the streaky structure. The spatial pattern of the disturbance development (Fig. 1a) shows that transverse meandering of the streaky structure is observed at the initial stage, which is typical for the development of sinusoidal instability. However, the structure of the disturbed downstream region of the flow is transformed to characteristic coherent structures similar to Λ vortices. The development of secondary disturbances is most clearly observed in the spatial pattern presented in Fig. 1b. At the initial stage of disturbance development, a pair of quasi-longitudinal, alternating-sign vortices is observed. Downstream of the flow, they are transformed to Λ structures, and the transverse scale of these coherent structures increases. Thus, detailed thermal anemometer measurements at the nonlinear stage of the development of sinusoidal instability show that the secondary high-frequency destruction of the streaky structure is associated with the formation of Λ structures, the destruction of which downstream of the flow leads to the turbulization of the flow.

Figure 2 shows patterns of the varicose destruction of the streaky structure. The spatial pattern of the disturbance development (Fig. 2a) shows that the longitu-

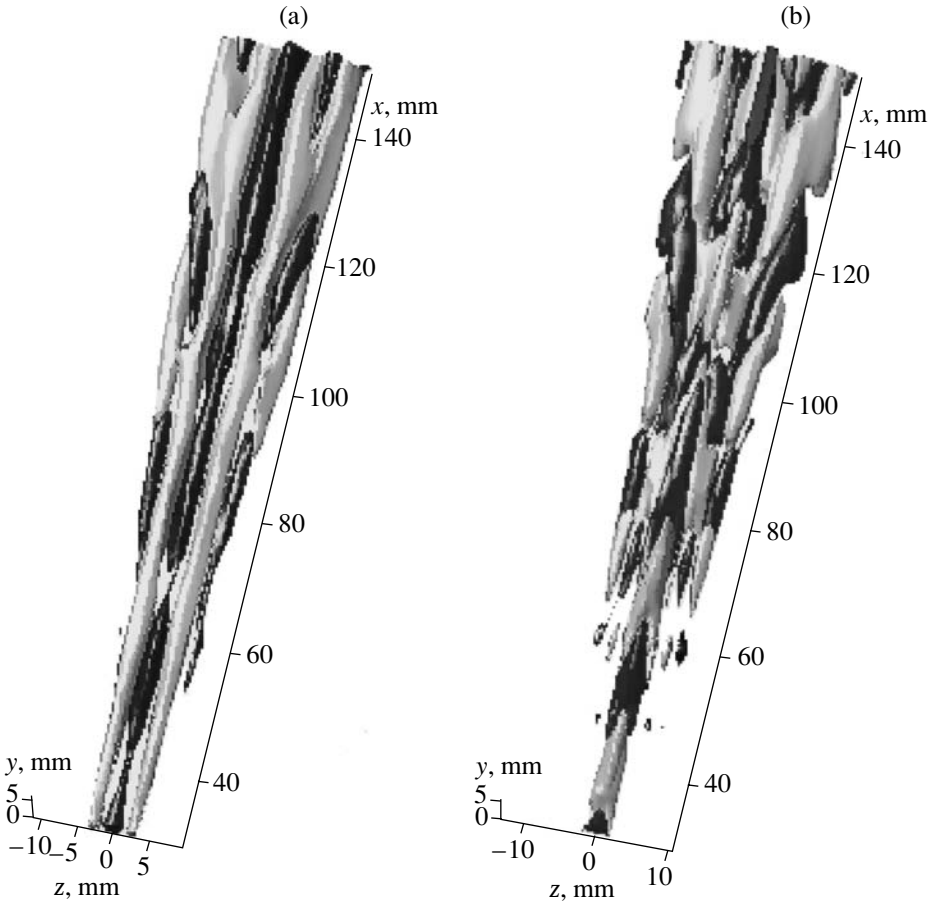

Fig. 2. Spatial patterns of the varicose destruction of the streaky structure: (a) the development of the secondary disturbance jointly with its effect on average velocity (minimum pulsation level 3.8% of U_∞) and (b) the development of the secondary high-frequency disturbance (minimum pulsation level 1.3% of U_∞). Dark and light grey tones are excesses and defects of velocity, respectively.

dinal modulation of the streaky structure by the secondary-disturbance frequency (f = 150 Hz) is observed at the initial section, which is typical of the development of varicose instability. However, the structure of the disturbed region further downstream of the flow is transformed to characteristic coherent structures similar to Λ vortices, as in the case of the sinusoidal destruction of the streaky structure. However, we emphasize that, in contrast to the latter case, Λ structures are asymmetric; i.e., the second counter-rotating vortex is at the formation stage due to weak vorticity at the transverse boundaries of the disturbance field. Below, symmetric Λ structures will be observed when considering the direct development of high-frequency disturbance.

We consider the dynamics of the direct development of secondary high-frequency disturbance generated on the streaky structure. The development of secondary disturbances is most clearly manifested in the spatial pattern shown in Fig. 2b. At the initial stage of disturbance development, a set of quasi-longitudinal vortices is observed, which is transformed downstream of the flow to hairpin vortices or Λ structures. These vortices are pronounced at z = 0 mm in the form of a pair of alternating-sign structures at each period of the secondary disturbance. As was mentioned above, Λ structures or hairpin vortices become asymmetric at $z = \pm 5$ mm (transverse boundaries of the disturbed region). Nevertheless, the structure of the second counter-rotating vortex of these coherent formations is evidently observed. We note that such coherent structures were observed in [2], where the nonlinear stage of varicose instability was studied. Investigations of the varicose instability of a single streaky structure in the boundary layer of the sliding wing [3] show that Λ vortices are transformed to asymmetric structures due to the transverse flow. Thus, detailed thermal anemometer measurements at the nonlinear stage of the development of varicose instability show that the secondary high-frequency destruction of the streaky structure is attributed to the formation of Λ structures, as in the case of the sinusoidal destruction of the streaky structure.

In conclusion, we emphasize that the scenario of classical laminar–turbulent transition at the nonlinear stage of this process is associated with the three-dimensional distortion of the two-dimensional Tollmien–Schlichting wave and the formation of three-dimen-

sional coherent structures of the Λ-vortex type. These investigations show that there are other scenarios for the occurrence of Λ structures in the near-wall shear flows, in particular, in the process of the secondary high-frequency instability of streaky structures of the sinusoidal and varicose types. The secondary high-frequency instability of streaky structures of the sinusoidal and varicose types at the nonlinear stage was found to lead to the multiplication of new streaky structures downstream of the flow. It has been established that the mechanism of the nonlinear destruction of the streaky structure through the development of secondary disturbance in it is associated with the formation of coherent structures of the Λ-vortex type for both sinusoidal and varicose types of instabilities. Λ vortices are shown to be multiplied in the transverse direction upon the evolution of disturbance downstream of the flow. It has been shown that varicose instability can exist on the sliding wing [3], rapidly transforming under the action of the secondary flow to the superposition of structures of sinusoidal and varicose instability.

This result is important for insights concerning both a mechanism of the turbulization of flows modulated by streaky structures and mechanisms of the reproduction of turbulence in turbulent flows, where the dynamics of coherent structures of the viscous sublayer plays a substantial role. The mechanism of the transformation of a Λ structure to a turbulent spot, particularly through the secondary high-frequency instability of its components—two counter-rotating vortices (legs of the structure)—is also well known [4]. At the same time, there are various methods for controlling the development of coherent structures such as Λ vortices, hairpin vortices, streaky structures, etc. As was shown in a number of works, riblets [1, 5–8], localized and distributed drainage [1, 8], transverse vibrations of the wall [9], etc., considerably affect both the intensity of coherent structures and their secondary instability, which can be used to control sinusoidal and varicose instability.

ACKNOWLEDGMENTS

This work was supported by the Russian Foundation for Basic Research (project no. 02-01-00006), the Council of the President of the Russian Federation for Support of Young Russian Scientists and Leading Scientific Schools (project no. NSh-964.2003.1), and Advanced Ship Engineering Research Center of the Korea Science and Engineering Foundation (KOSEF).

REFERENCES

1. A. V. Boiko, G. R. Grek, A. V. Dovgal, and V. V. Kozlov, *The Origin of Turbulence in Near-Wall Flows* (Springer-Verlag, Berlin, 2002).
2. M. Asai, M. Minagawa, and M. Nishioka, J. Fluid Mech. **455**, 289 (2002).
3. Yu. A. Litvinenko, G. R. Grek, V. V. Kozlov, *et al.*, Teplofiz. Aéromekh. **11** (1), 1 (2004).
4. G. R. Grek, V. V. Kozlov, M. M. Katasonov, and V. G. Chernorai, Curr. Sci. **79**, 781 (2000).
5. G. R. Grek, V. V. Kozlov, and S. V. Titarenko, J. Fluid Mech. **315**, 31 (1996).
6. G. R. Grek, V. V. Kozlov, and S. V. Titarenko, Rech. Aerosp., No. 1, 1 (1996).
7. G. R. Grek, V. V. Kozlov, B. G. B. Klingmann, and S. V. Titarenko, Phys. Fluids **7**, 2504 (1995).
8. V. V. Kozlov and G. R. Grek, in *Lectures Notes in Physics. Physics of Rotating Fluids*, Ed. by C. Egbers and G. Pfister (Springer-Verlag, Berlin, 2000), pp. 375–394.
9. M. M. Katasonov and V. V. Kozlov, Izv. Akad. Nauk, Ser. Mekh. Zhidk. Gaza **34** (5), 63 (1999).

Translated by R. Tyapaev

Doklady Physics, Vol. 50, No. 3, 2005, pp. 151–153. Translated from Doklady Akademii Nauk, Vol. 401, No. 2, 2005, pp. 193–195.

MECHANICS

Effect of Non-Coulomb Dry Friction on the Stability of Automatic Systems

V. N. Shamberov

Presented by Academician N.F. Morozov February 14, 2004

Received May 20, 2004

It has been established that the dry friction (as a non-Coulomb dry friction model) in a direct action regulator (Vyshnegradskii problem) with a self-restoring object causes self-oscillations in the system. Therefore, the common opinion that dry friction in the Vyshnegradskii problem does not change the conclusion of unlimited stability, which was obtained from linear analysis, remains correct only for the Coulomb dry friction model.

The majority of investigations of the effect of dry friction on the stability of control systems were performed for a simplified model of dry friction, the so-called Coulomb friction, which ignores the excess of static friction over sliding friction in the dry friction law (Fig. 1a).[1] However, there are examples of exciting oscillations that cannot be described by the Coulomb friction law.

Let us bring the problem into focus by means of an example of the well-known Vyshnegradskii problem, which is the main problem associated with the effect of dry friction in a direct action regulator on the stability of control systems.[2] This problem has been described sequentially in a number of works [2, 3]. The main conclusion is as follows: when the object is absolutely stable, Coulomb friction in the regulator does not generate oscillations but promotes the stability of the system, thus extending the area of the stability of equilibrium states due to the appearance of an area of "conditional" stability, in addition to the area of stability "on the whole" [2, 3].

Free oscillations corresponding to the Vyshnegradskii problem for a dynamical system, with the non-Coulomb dry friction model taken into consideration, can be described by the equations

$$T_a\dot{\varphi} + \delta_a\varphi = -\mu; \tag{1}$$

$$T_{p2}^2\ddot{\mu}$$

$$= \begin{cases} 0, \text{ if } |\varphi + T_{p3}\dot{\varphi} - T_{p1}\dot{\mu} - \delta_p\mu| < \dfrac{\varepsilon'}{2} \text{ or} \\ \text{if } \dot{\mu} = 0 \text{ and } \dfrac{\varepsilon'}{2} \le |\varphi + T_{p3}\dot{\varphi} - \delta_p\mu| < \dfrac{\varepsilon}{2}; \\ \varphi + T_{p3}\dot{\varphi} - \delta_p\mu - \dfrac{1}{2}\varepsilon\operatorname{sgn}(\varphi + T_{p3}\dot{\varphi} - \delta_p\mu), \\ \text{if } \dot{\mu} = 0 \text{ and } |\varphi + T_{p3}\dot{\varphi} - \delta_p\mu| \ge \dfrac{\varepsilon}{2}; \\ \varphi + T_{p3}\dot{\varphi} - T_{p1}\dot{\mu} - \delta_p\mu - \dfrac{1}{2}\varepsilon'\operatorname{sgn}\dot{\mu}, \\ \text{if } \dot{\mu} \ne 0 \text{ and } \dfrac{\varepsilon'}{2} < |\varphi + T_{p3}\dot{\varphi} - T_{p1}\dot{\mu} - \delta_p\mu|. \end{cases} \tag{2}$$

Equations (1) and (2) correspond to the dynamics of the controlled object and regulator, respectively, and a dot over a symbol stands for time differentiation. All terminology and definitions are given in accordance with [3]. The difference from the corresponding defini-

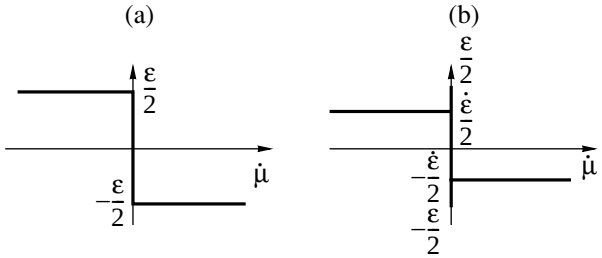

Fig. 1. Different approximations of the dry friction law.

[1] The term "Coulomb friction" for the simplest approximation of the dry friction law has emerged quite inexplicably: S.A. de Coulomb (1736–1806) was the first who determined the existence of dry friction static forces, which exceed sliding forces.

[2] Classification of automatic control systems according to their definitions (that is, the presence or absence of an amplifier in the system) does not have an adequate mathematical correspondence.

St. Petersburg State Marine Technical University, ul. Lotsmanskaya 3, St. Petersburg, 190008 Russia
e-mail: shamberov@mail.ru

1028-3358/05/5003-0151$26.00

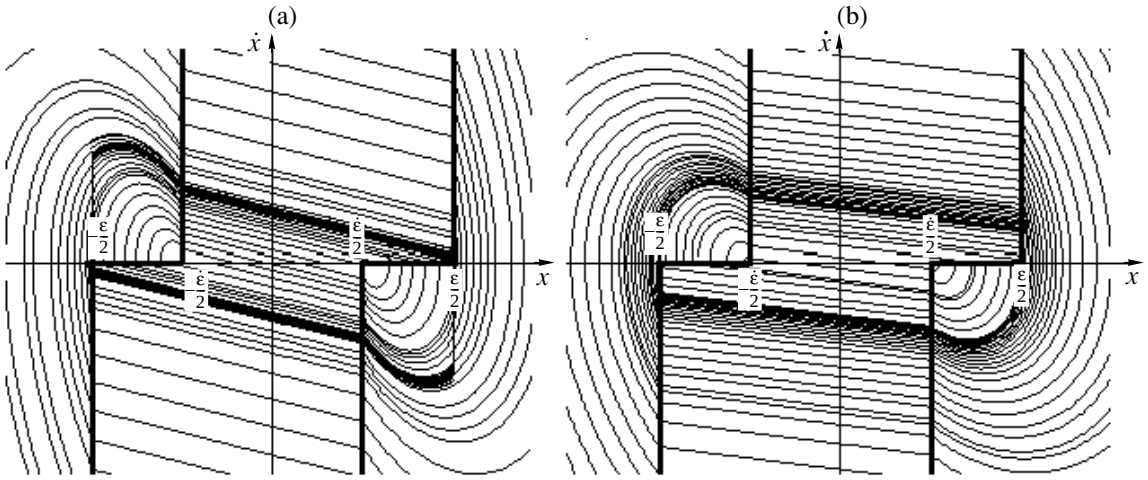

Fig. 2. Phase portrait.

tions [2, 3] is that the excess of state friction forces (parameter ε) over sliding friction forces (parameter $\varepsilon' < \varepsilon$) is now taken into consideration (Fig. 1b). In the limiting case (when $T_{p2}^2 \longrightarrow 0$), we get a so-called "degenerate model" (when $T_{p2} = 0$) of the dynamic regulator:

$$T_{p1}\dot{\mu} = \begin{cases} 0, \text{ if } |\varphi + T_{p3}\dot{\varphi} - \delta_p\mu| < \dfrac{\varepsilon'}{2}, \text{ or } \dot{\mu}^- = 0 \text{ and } \dfrac{\varepsilon'}{2} \le |\varphi + T_{p3}\dot{\varphi} - \delta_p\mu| < \dfrac{\varepsilon}{2}; \\ \varphi + T_{p3}\dot{\varphi} - \delta_p\mu - \dfrac{1}{2}\varepsilon\,\mathrm{sgn}(\varphi + T_{p3}\dot{\varphi} - \delta_p\mu), \text{ if } \dot{\mu}^- = 0 \text{ and } |\varphi + T_{p3}\dot{\varphi} - \delta_p\mu| \ge \dfrac{\varepsilon}{2}; \\ \varphi + T_{p3}\dot{\varphi} - \delta_p\mu - \dfrac{1}{2}\varepsilon'\,\mathrm{sgn}(\dot{\mu}^-), \text{ if } \dot{\mu}^- \ne 0 \text{ and } \dfrac{\varepsilon'}{2} < |\varphi + T_{p3}\dot{\varphi} - \delta_p\mu|, \end{cases} \quad (3)$$

where $\dot{\mu}^-$ is the pre-historical state. The legality of the transformation, which was earlier known as the "jump hypothesis," is based on arguments given by A.N. Tikhonov, L.S. Pontryagin, E.F. Mishchenko, *et al.* in the theory of relaxation oscillations [4].

In contrast to the detailed model given by Eqs. (1) and (2), the initial conditions $\dot{\mu}_0$ for the degenerated model should be compatible with the description given by Eq. (3). The presence of a limited cycle (self-oscillations) in the space of states (three-sheeted phase plane) was determined in [5] by the point transformation of the segment

$$x = \frac{\varepsilon}{2}, \quad 0 \ge \dot{x} \ge (T_a\delta_p + T_{p3})\frac{\varepsilon' - \varepsilon}{2T_aT_{p1}},$$

where $x = T_{p3}\dot{\varphi} + \varphi - \delta_p\mu$. The second transformation is an inverse point transformation of a symmetric segment

$$x = -\frac{\varepsilon}{2}, \quad 0 \le \dot{x} \le (T_a\delta_p + T_{p3})\frac{\varepsilon - \varepsilon'}{2T_aT_{p1}}$$

into the points of the half-line $x = \dfrac{\varepsilon'}{2}$, $\dot{x} < 0$ (Fig. 2a). Finally, the point transformation of the half-line $x > \dfrac{\varepsilon}{2}$, $\dot{x} = 0$ and a backward point transformation of the symmetric half-line $x < -\dfrac{\varepsilon}{2}$, $\dot{x} = 0$ into the points of the half-line $x = \dfrac{\varepsilon'}{2}$, $\dot{x} < 0$ are performed (Fig. 2b).

The limited cycle appears from the points $\dot{x} = 0$ and $|x| = \dfrac{\varepsilon}{2}$ of the equilibrium segment $\dot{x} = 0, |x| \le \dfrac{\varepsilon}{2}$, if (at $A > 1$ and $A \le D \le A + 1$) the condition

$$(A + 1 - D)Q > (D - 1)\exp\left(-\frac{A}{A-1}\ln\frac{D-1}{D-A}\right)$$

is broken, and if (at $A_1 > 0$) the condition

$$(2 - D)Q > \sqrt{(1 - D)^2 + A_1^2}\exp\left[-\frac{1}{A_1}\left(\arctan\frac{1 - D}{A_1} + \frac{\pi}{2}\right)\right]$$

is broken, or (at $A = 1$, $A_1 = 0$) the condition

$$(2 - D)Q > (D - 1)\exp\left(-\frac{1}{D - 1}\right)$$

is broken. The generalized parameter $Q = \dfrac{\varepsilon + \varepsilon'}{\varepsilon - \varepsilon'}$ characterizes the non-Coulomb dry friction in the regulator. The other parameters can be defined as:

$$A_1 = -\frac{\beta}{\alpha}, \quad A = \frac{\alpha_1}{\alpha}, \quad D = -\frac{\delta_p T_a + T_{p3}}{T_{p1} T_a \alpha}.$$

Here, β and α are, respectively, the imaginary and real parts of complex conjugate roots, and $\alpha = \lambda_1$ and $\alpha_1 = \lambda_2$ are the real roots ($\alpha > \alpha_1$) of the equation

$$T_a T_{p1}\lambda^2 + (\delta_a T_{p1} + \delta_p T_a + T_{p3})\lambda + (1 + \delta_a \delta_p) = 0.$$

The above results prove the presence of self-oscillations in the system described by Eqs. (1) and (2) for the region of the parameters (when $\delta_a > 0$), where roots λ_1, λ_2, and λ_3 of the equation

$$T_a T_{p2}^2 \lambda^3 + (\delta_a T_{p2}^2 + T_a T_{p1})\lambda^2 + (\delta_a T_{p1} + \delta_p T_a + T_{p3})\lambda + (1 + \delta_a \delta_p) = 0$$

are real negative roots or where two of them are complex conjugate roots with a negative real part that is larger than the real root.

The above results were confirmed in [6], where the system of Eqs. (1) and (2) with $T_{p2}^2 > 0$ and $\delta_a \geq 0$ was investigated by the methods of real and computer experiments. These conclusions are consistent with the Ishlinsky–Kragelsky theory, which attributes the excess of dry friction static forces over sliding forces to long-term immobility [7].

REFERENCES

1. C. A. Coulomb, Mem. Math. Phys. Acad. Sci. **10**, 161 (1785).
2. A. A. Andronov and A. G. Maĭer, Dokl. Akad. Nauk SSSR **47** (5), 345 (1945).
3. A. A. Tal', Avtom. Telemekh. **14**, 604 (1953).
4. *Differential Equations with a Small Parameter and Relaxation Oscillations*, Ed. by E. F. Mishchenko and N. Kh. Rozov (Nauka, Moscow, 1975; Plenum, New York, 1980).
5. V. N. Shamberov, Candidate's Dissertation in Engineering (Leningrad, 1988).
6. S. A. Sogonov, Candidate's Dissertation in Engineering (St. Petersburg, 1999).
7. A. Yu. Ishlinskiĭ and I. V. Kragel'skiĭ, Zh. Tekh. Fiz. **14** (4/5), 276 (1944).

Translated by V. Shamberov

Doklady Physics, Vol. 50, No. 3, 2005, pp. 154–157. Translated from Doklady Akademii Nauk, Vol. 401, No. 3, 2005, pp. 337–341.

MECHANICS

Calculation of Potential Flows

K. N. Anakhaev

Presented by Academician M.Ch. Zalikhanov October 25, 2004

Received July 1, 2004

Methods for calculating potential flows based on the theory of functions of a complex variable have been widely used as fundamental investigation methods in many fields of engineering, including seepage theory, elasticity theory, continuum mechanics, heat dynamics, aero- and hydromechanics, electromagnetism, electro- and radio engineering, etc. [1–3]. In most cases, the application of these methods involves conformal mapping of the rectangle *1–2–3–4* of the complex domain $W = \varphi + i\psi$ (Fig. 1a) onto a complex half-plane $\zeta = \xi + i\eta$ (Fig. 1b). It is well known [1–5] that this mapping is performed by means of Jacobi elliptic functions, making use of the complete elliptic integrals of the first kind K and K' (Fig. 1) with the modulus λ and the complementary modulus $\lambda' = \sqrt{1-\lambda^2}$, respectively. This generates considerable difficulties due to the necessity of series expansion of elliptic functions, interpolation of special nonograms and tables, solution of inverse table problems, etc., particularly when it comes to determining the current values of Jacobi functions for the rectangle interior [1–4, 6, 7]. Moreover, the difficulty of expressing the elliptic functions in terms of elementary functions restricts the possibility of analytically representing the relationship between the physical parameters of the problem under consideration and the given boundary conditions, as well as the use of complicated calculation techniques.

The above circumstances considerably constrain the further development of analytical methods for investigating engineering problems in the above-listed lines of inquiry. In this study, we present a new method for solving this problem based on the conformal mapping of a rectangle, one side of which has a vanishingly small convexity, onto a half-plane by means of elementary functions. For this purpose, in the complex half-band $W = \varphi + i\psi$ of width H (Fig. 2), we introduce the function

$$\psi = \frac{H}{\pi}\operatorname{arcsinh}\sqrt{R^2 - \sin^2\frac{\pi\varphi}{H}}, \qquad (1)$$

where φ and ψ are the current coordinates, and $R \geq 1$ is a parameter determining a family of symmetric curves $\psi = f(\varphi)$ that is orthogonal to the lateral sides of the half-band and has a convexity in their central part. The values of function (1) on the half-band boundaries *1–4* and *2–3* and on the 0ψ axis are determined at $\varphi = \pm\frac{H}{2}$ and $\varphi = 0$, respectively:

$$\begin{aligned} &\text{points } 3 \text{ and } 4\text{: } \psi_{3,4} = \frac{H}{\pi}\operatorname{arcosh} R = Q; \\ &\text{point } A\text{: } \psi_A = \frac{H}{\pi}\operatorname{arcsinh} R. \end{aligned} \qquad (2)$$

From Eq. (2) we determine the parameter

$$R = \cosh\frac{\pi Q}{H}. \qquad (3)$$

For $\psi_{3,4} = Q = H$ (correspondingly, $R = \cosh\pi = 11.59195$),

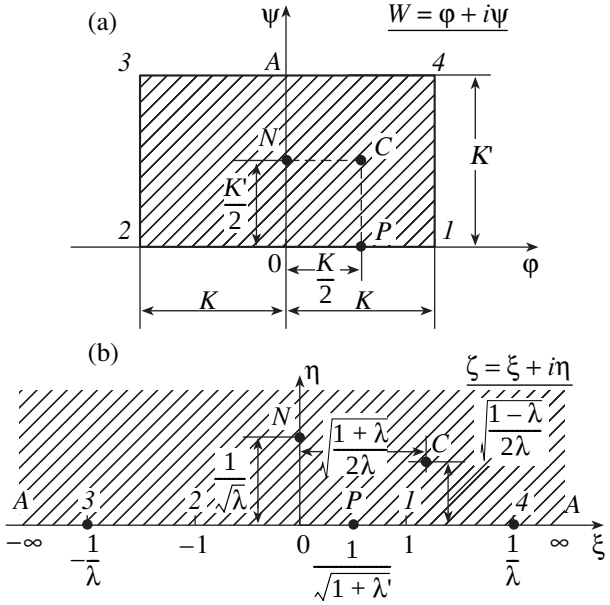

Fig. 1. Exact conformal mapping of a rectangle onto a half-plane using Jacobi elliptic functions: (a) rectangle *1–2–3–4* in the complex domain $W = \varphi + i\psi$ and (b) complex half-plane $\zeta = \xi + i\eta$, where K and K' are complete elliptic integrals of the first kind with the modulus λ and the complementary modulus $\lambda' = \sqrt{1-\lambda^2}$, respectively.

Kabardino-Balkar State Agricultural Academy, ul. Tolstogo 185, Nalchik, 360004 Russia
e-mail: agron@kbr.net.ru

1028-3358/05/5003-0154$26.00

the ordinate of point A is equal to

$$\psi_A = \frac{H}{\pi}\operatorname{arcsinh}(\cosh\pi) = 1.00118H,$$

that is, the curve *3–A–4* is almost coincident with the straight line *3–4* (the maximum error at point A is equal to 0.118%). Therefore, figure *1–2–3–A–4* can be treated with fairly high accuracy as a rectangle with equal sides (square). With further increase in the vertical side of the rectangle, i.e., the value of Q, the convexity at point A relative to line *3–4* becomes vanishingly small: it is equal to 0.01, 0.001, and 0.0001% for $\frac{Q}{H} =$ 1.35, 1.67, and 2, respectively.

The main feature of curves (1) is that domains *1–2–3–A–4* in the half-band $W = \varphi + i\psi$ (Fig. 3a) bounded by the curves and treated as "elongated" rectangles for $\frac{Q}{H} \geq 1 \left(\text{or } \frac{K'}{K} \geq 2 \right)$ can be rigorously mapped onto a semicircle of radius R in a complex domain $\varepsilon = \varepsilon_1 + i\varepsilon_2$ (Fig. 3b) by means of the function

$$\varepsilon = \sin\frac{\pi W}{H}. \tag{4}$$

Further mappings of this semicircle onto the half-plane $\zeta = \xi + i\eta$ (Figs. 3b–3g) are performed using the functions

$$t = \frac{\varepsilon}{R}, \quad \zeta = \frac{1}{t}, \quad \zeta_0 = 0.5\left(\zeta_1 + \frac{1}{\zeta_1}\right), \qquad \zeta^* = \frac{1}{\zeta_0}, \quad \zeta = \frac{\zeta^*}{\lambda}, \tag{5}$$

where

$$\lambda = \frac{2R}{R^2 + 1} \tag{6}$$

is the inverse of the point-*1* image on the half-plane $\zeta_0 = \xi_0 + i\eta_0$ (Fig. 3e) and corresponds to the modulus of the complete elliptic integral of the first kind K.

After the transformations, we obtain a function conformally mapping the "elongated" rectangle $\frac{Q}{H} \geq 1 \left(\text{or } \frac{K'}{K} \geq 2 \right)$ *1–2–3–A–4* of the domain $W = \varphi + i\psi$ onto the half-plane $\zeta = \xi + i\eta$ in the form

$$\zeta = \frac{2}{\lambda R}\frac{\sin\frac{\pi W}{H}}{1 + R^{-2}\sin^2\frac{\pi W}{H}}. \tag{7}$$

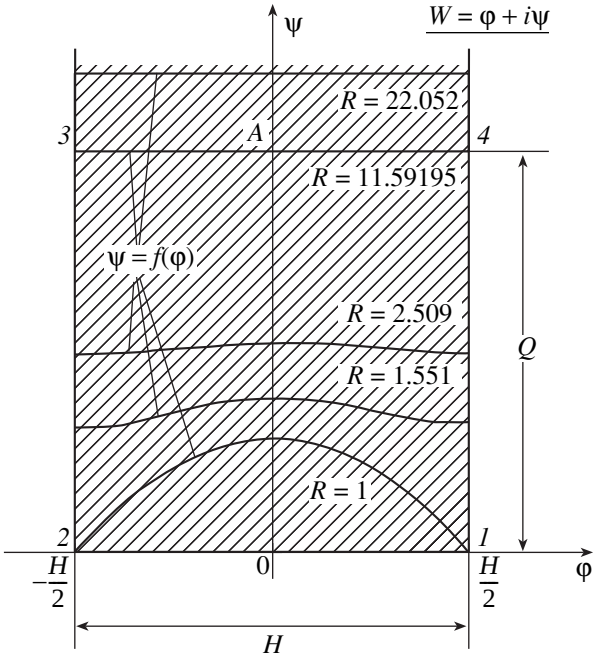

Fig. 2. Plots of the function $\psi = \frac{H}{\pi}\operatorname{arcsinh}\sqrt{R^2 - \sin^2\frac{\pi\varphi}{H}}$ in the complex half-band $W = \varphi + i\psi$.

Since $R \geq 11.59195$ in this case (correspondingly, $R^2 \geq 134.373$), unity can be neglected in the denominator of Eq. (6). Then, we have

$$\lambda \approx \frac{2}{R}, \tag{8}$$

while dependence (7) takes the simpler form

$$\zeta = \frac{\sin\frac{\pi W}{H}}{1 + R^{-2}\sin^2\frac{\pi W}{H}}. \tag{9}$$

From Eqs. (6) and (8), the parameter R can be expressed as follows:

$$R = \frac{1 + \sqrt{1 - \lambda^2}}{\lambda} \approx \frac{2}{\lambda}. \tag{10}$$

For the particular case of a rectangle with an infinitely long vertical side (half-band), when $\frac{Q}{H} \longrightarrow \infty$, formulas (7) and (9) provide the conformal mapping of the half-band onto a half-plane in the form $\zeta = \sin\frac{\pi W}{H}$,

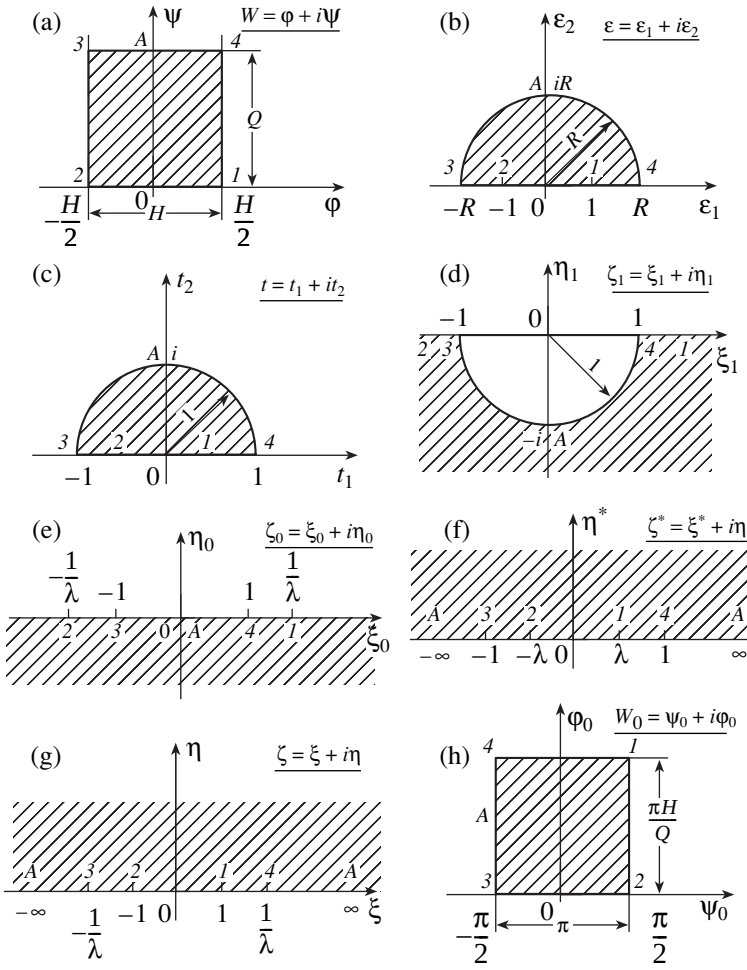

Fig. 3. Diagram of successive conformal mappings $W = \varphi + i\psi$ of the complex domain *1–2–3–A–4* onto the complex half-plane $\zeta = \xi + i\eta$.

which completely coincides with the known exact solution [1, 2, 4, 5].

A rectangle "broadened" along the real axis 0φ, $\frac{Q}{H} < 1$ $\left(\text{or } \frac{K'}{K} < 2\right)$ is conformally mapped onto the half-plane $\zeta = \xi + i\eta$ using an additional intermediate complex π-wide domain $W_0 = \varphi_0 + i\psi_0$ (Fig. 3h) determined by the function

$$W_0 = \frac{\pi}{2} + i\pi\left(W + \frac{H}{2}\right)Q^{-1}, \qquad (11)$$

which rotates and extends the "broadened" rectangle along the imaginary axis $0\varphi_0$, as shown in Fig. 3h. Its further successive conformal mappings onto the half-plane $\zeta = \xi + i\eta$ (Fig. 3g) are performed similarly. As a result, we obtain the mapping function

$$\zeta = \frac{(\zeta^* - n)(1 - m)}{\zeta^*(1 + m - 2n) + n(1 + m) - 2m};$$

$$\zeta^* = \frac{2}{r}\frac{\cosh\left[\frac{\pi}{Q}\left(W + \frac{H}{2}\right)\right]}{1 + r^{-2}\cosh^2\left[\frac{\pi}{Q}\left(W + \frac{H}{2}\right)\right]}, \qquad (12)$$

$$r = \cosh\frac{\pi H}{Q}, \quad m = \frac{2r}{r^2 + 1},$$

$$n = \frac{2}{r}\frac{\cosh\frac{0.5\pi H}{Q}}{1 + r^{-2}\cosh^2\frac{0.5\pi H}{Q}}.$$

Thus, functions (7), (9), and (12) conformally map the "elongated" $\left(\frac{Q}{H} \geq 1\right)$ and "broadened" $\left(\frac{Q}{H} < 1\right)$ rectangles, respectively, onto the half-plane $\zeta = \xi + i\eta$ (Fig. 3g).

A comparison of the results of calculations according to formulas (7), (9), and (12) gives almost complete

coincidence with the exact values. Maximum errors in a narrow range of the rectangle side ratio, when $\frac{Q}{H} \longrightarrow 1$ (i.e., for near-square shapes), are not greater than 0.60–0.65%.

The above presentation provides grounds for recommending formulas (7), (9), and (12) in the interest of improving the available and developing new, nearly exact methods of calculation in different fields of engineering. They make it possible to consider a rich variety of engineering problems associated with the mapping of rectangles onto a half-plane, which were previously solved using Jacobi elliptic functions, on the basis of elementary functions, while using the advantages provided by rigorous analytical methods.

We will consider the use of the solution suggested in engineering problems with reference to the example of high-pressure water seepage through a permeable foundation of depth T below a plane shallow apron with a length of L. The exact value of the reduced (specific) seepage rate Q under such a structure is equal to [2, 4, 5, 7]

$$Q = \frac{Q_n}{k} = \frac{0.5HK'}{K}, \quad (13)$$

where K and K' are the complete elliptic integrals of the first kind with, respectively, the modulus

$$\lambda = \tanh\frac{0.25\pi L}{T} \quad (14)$$

and the complementary modulus $\lambda' = \sqrt{1-\lambda^2}$, H is the water head acting on the structure, Q_n is the (specific) seepage rate under actual conditions [4], and k is the soil permeability of the base.

The expressions for determining the reduced seepage rate Q on the basis of dependences (9) and (12) for the cases $\frac{Q}{H} \geq 1$ and $\frac{Q}{H} < 1$, i.e., for $\frac{T}{L} \geq 0.25\pi \operatorname{arctanh}^{-1}\frac{2}{\cosh\pi} \approx 4.51$ and $\frac{T}{L} < 4.51$, are as follows:

for $\frac{Q}{H} < 1 \left(\frac{T}{L} < 4.51\right)$

$$Q = \frac{\pi H}{\operatorname{arccosh}[F(F+\sqrt{F^2+2})]}, \quad (15)$$

where $F = \frac{0.5(1+\sqrt{\sqrt{\lambda}})^2}{1-\sqrt{\lambda}}$, and

for $\frac{Q}{H} \geq 1 \left(\frac{T}{L} \geq 4.51\right)$

$$Q = \frac{H}{\pi}\operatorname{arccosh}\frac{2}{\lambda}. \quad (16)$$

A comparison of the seepage rates Q through the permeable base of a limited depth T of the plane L-long apron calculated by formulas (15) and (16) with the exact values given by Eqs. (13) for $H = 1$ and $k = 1$ (in conditional units) yields an almost complete coincidence of results (the maximum error is 0.1–0.2%). Moreover, the method proposed above provides the solution for the particular case of an infinitely deep permeable base ($T \longrightarrow \infty$). For example, the head h acting along the basement of this plane apron is obtained in the form

$$h = \frac{H}{\pi}\arccos\frac{2x}{L}, \quad (17)$$

where $-\frac{L}{2} \leq x \leq \frac{L}{2}$ is the abscissa of a point on the apron basement, which completely coincides with the result of the rigorous hydromechanical solution obtained by N. N. Pavlovskiĭ for this case [2, 4, 5, 7].

Thus, the solution obtained above makes it possible to determine all required parameters of a seepage flow at any point of the flow region, which would be hardly realizable using Jacobi elliptic functions [2, 4, 5]. The results of this study can be used for refining the available and developing new fundamental methods for studying potential flows associated with conformal mappings of a rectangle onto a half-plane in different fields of engineering. Deriving highly accurate and simple dependences provides deeper insight into the internal relationships and the current characteristics of the problem under study including the case of more complicated calculation schemes.

REFERENCES

1. W. von Koppenfels and F. Stallmann, *Praxis der konformen Abbildung* (Springer, Berlin, 1957; Inostrannaya Literatura, Moscow, 1963).
2. V. I. Lavrik, V. P. Fil'chakova, and A. A. Yashin, *Conformal Mappings of Physical Topological Models* (Naukova Dumka, Kiev, 1990) [in Russian].
3. P. F. Fil'chakov, *Handbook on Superior Mathematics* (Naukova Dumka, Kiev, 1973) [in Russian].
4. N. N. Pavlovskiĭ, *Selected Works*, Vol. 2: *Ground Water Flows* (Izd. Akad. Nauk SSSR, Moscow and Leningrad, 1956) [in Russian].
5. P. Ya. Polubarinova-Kochina, *Theory of Ground Water Flows* (Nauka, Moscow, 1977) [in Russian].
6. I. S. Gradshteyn and I. M. Ryzhik, *Tables of Integrals, Series, Sums, and Products* (Nauka, Moscow, 1971; Academic Press, New York, 1980).
7. *Handbook on Hydraulic Engineering* (Gosstroĭizdat, Moscow, 1955) [in Russian].

Translated by M. Lebedev

Doklady Physics, Vol. 50, No. 3, 2005, pp. 158–160. Translated from Doklady Akademii Nauk, Vol. 401, No. 3, 2005, pp. 342–344.

MECHANICS

Vibrations and Stability of a Viscoelastic Strip Placed into Gas Flow

I. A. Kiĭko[1] and V. V. Pokazeev[2]

Presented by Academician D.M. Klimov June 7, 2004

Received July 14, 2004

Flutter of viscoelastic rectangular plates was first investigated in [1–3]. The results of those studies were based on both the Bubnov–Galerkin and averaging methods [4]. It was found that the critical flow velocity was lower by a factor of approximately 2 than that of the corresponding elastic plate with an instant Young's modulus, the ratio between the velocities being independent of the viscous properties of the material. In [5], a seemingly natural result was reported concerning asymptotic stability. It was estimated that in the case of low viscosity, flow velocity found according to the ultimate modulus provides the sufficient condition for the stability of vibrations. In the present study, we deal with a crucial new result based on one exact and one approximate solution to the problem of the flutter of a viscoelastic strip. We have established that critical velocity is equal to that corresponding to the instant Young's modulus, and viscous properties of the material affect the character of strip motion only in the subcritical region.

FORMULATION OF THE PROBLEM

We consider a rectangular coordinate system in which a strip occupies the domain $0 \le y \le l$ and $|x| < \infty$. Gas flowing around the strip on one side is characterized by the velocity vector $\mathbf{v} = v\mathbf{n}_0$ ($\mathbf{n}_0 = \{\cos\theta, \sin\theta\}$) and by the unperturbed parameters p_0, ρ_0 and a_0 (pressure, density, and sound velocity, respectively). The strip is made of a linear viscoelastic material. The strain–stress relation has the form

$$\sigma = E_0\left(\varepsilon(t) - \varepsilon_0\int_0^t \Gamma(t-\tau)\varepsilon(\tau)d\tau\right) \equiv E_0(1-\varepsilon_0\hat{\Gamma}_1)\varepsilon(t);$$

where E_0 is the instant modulus and ε_0 is the viscosity parameter.

Strip vibrations are described by the equation [6, 7]

$$D_0(1-\varepsilon_0\hat{\Gamma}_1)\Delta^2 w + \rho h\frac{\partial^2 w}{\partial t^2} + \frac{\gamma p_0}{a_0}\left(\frac{\partial w}{\partial t} + v\mathbf{n}_0\cdot\operatorname{grad} w\right) = 0. \quad (1)$$

Here, $D_0 = \dfrac{E_0 h^3}{12-\nu}$, h is the strip thickness, γ is the polytropic exponent, ρ is the density of the material, and υ is the constant Poisson's ratio. Equation (1) is investigated under the boundary conditions of a pin-edge fixing:

$$y = 0, \quad w = 0, \quad \frac{\partial^2 w}{\partial y^2} = 0; \qquad y = l, \quad w = 0, \quad \frac{\partial^2 w}{\partial y^2} = 0 \quad (2)$$

and for initial conditions determined by the type of perturbation. The problem consists in the necessity of finding the minimum value of flow velocity v_{cr} such that the perturbed motion is stable at $\upsilon < \upsilon_{cr}$ and unstable at $\upsilon > \upsilon_{cr}$.

We now assume that $\Gamma(t) = \exp(-\beta t)$. Upon introducing the dimensionless variables, namely, coordinates $\frac{x}{l}$, $\frac{y}{l}$, time βt, and velocity $M = \dfrac{\upsilon}{a_0}$ (under conservation of other previous notation), Eq. (1) takes the form

$$(1-\lambda\Gamma_1)\Delta^2 w + a_3 M n_0\cdot\operatorname{grad} w + a_2\frac{\partial w}{\partial t} + a_1\frac{\partial^2 w}{\partial t^2} = 0. \quad (3)$$

[1] *Moscow State University, Vorob'evy gory, Moscow, 119899 Russia*

[2] *Moscow State Technical University "MAMI," ul. Bol'shaya Semenovskaya 38, Moscow, 105839 Russia*

e-mail: mami_hpvv@mtu-net.ru

1028-3358/05/5003-0158$26.00

Here,

$$a_1 = 12(1-\nu^2)\frac{\beta^2 l^4 \rho}{h^2 E_0}, \quad a_2 = 12(1-\nu^2)\frac{\beta l^4 \gamma p_0}{h^3 a_0 E_0},$$

$$a_3 = 12(1-\nu^2)\frac{\gamma p_0}{E_0}\left(\frac{l}{h}\right)^3, \quad \lambda = \frac{\varepsilon_0}{\beta}; \quad \Gamma = e^{-t}.$$

LONGITUDINAL FLOW AROUND THE STRIP

In the case $\theta = 0$, a perturbation bounded at infinity and satisfying conditions (2) is chosen in the form

$$t = 0, \quad w = c_1 \exp(-i\alpha x)\sin\pi y,$$

and

$$\frac{\partial w}{\partial t} = c_2 \exp(-i\alpha x)\sin\pi y \quad (\alpha \in R).$$

In accordance with the above conditions, we take

$$w = A(t)\exp(-i\alpha x)\sin\pi y.$$

Next, substituting this expression into (3) and passing to the Laplace image, we arrive at

$$L(A(t)) = \frac{p_2(s)}{p_3(s)},$$
$$p_2(s) = (s+1)(a_1 c_1 s + a_1 c_2 + a_2 c_1), \qquad (4)$$
$$p_3(s) = a_1 s^3 + (a_1 + a_2)s^2$$
$$+ (\mu + a_2 - i\alpha a_3 M)s + (1-\lambda)\mu - i\alpha a_3 M$$

(s is the transformation parameter). The original of image (4) is reconstructed in the conventional manner:

$$A(t) = A_1 e^{s_1 t} + A_2 e^{s_2 t} + A_3 e^{s_3 t},$$
$$A_m = \frac{(1+s_m)\left(c_2 + c_1\left(\frac{a_2}{a_1} + s_m\right)\right)}{(s_m - s_j)(s_m - s_k)}, \qquad (5)$$
$$m \neq k, \quad m \neq j, \quad k \neq j.$$

In formulas (5), s_m are the roots of the equation $p_3(s) = 0$ and $\mu = (\alpha^2 + \pi^2)^2$. Solution (5) exponentially decreases (being asymptotically stable) if $\mathrm{Re}\, s_m < 0$ for an arbitrary m. At the same time, the solution is asymptotically unstable if one of the roots has $\mathrm{Re}\, s_m > 0$. The condition $\mathrm{Re}\, s_m = 0$ corresponds to the boundary between the stable and unstable domains provided that the remaining two roots lie in the left half-plane.

As our calculations indicate, at $M = 0$ (free vibrations), $\mathrm{Re}\, s_m < 0$ ($\forall m$); with a rise in M, one of the roots (let it be s_1) most rapidly approaches the imaginary axis and, at a certain M^*, becomes purely imaginary. The values of both $s_1^* = iy$ and M^* can be easily found from the equation $p_3(iy) = 0$. As a result, we arrive at

$$M^* = \frac{(\mu + a_2 - a_1 y^2)y}{\alpha a_3}.$$

Instead of y, the positive root of the biquadratic equation

$$y^4 - \left(\frac{\mu}{a_1} - 1\right)y^2 - (1-\lambda)\frac{\mu}{a_1} = 0$$

should be substituted into this equation.

The dimensionless velocity M^* depends on the wave formation parameter α. By definition, we take $M_{cr} = M^*(\alpha_{cr})$, where α_{cr} is found from the condition $\min_\alpha M^*$.

Table 1 presents the data of specific calculations for a number of parameters:

$\frac{p_0}{E_0} = 5 \times 10^{-7}$, $\rho = 8 \times 10^3$ kg m^{-3}, $\gamma = 1.4$, $\nu = 0.3$, $a_0 = 330$ m s^{-1}, and $\frac{l}{h} = 3 \times 10^2$. In all cases, it turned out that $\alpha_{cr} = \pi$ with an accuracy to the fourth significant figure after the decimal point.

Table 1

β	M_{cr}			
	$\lambda = 0$	$\lambda = 0.1$	$\lambda = 0.2$	$\lambda = 0.3$
0.1	0.096029	0.096065	0.096102	0.096138
0.01	0.096029	0.096033	0.096037	0.096040

The velocity being evaluated by the formula $M_{cr}^{el} = \frac{2\pi a_2}{a_3\sqrt{a_1}}$ and having the instant Young's modulus corresponds to $\lambda = 0$.

A crucial result follows from the data given in Table 1: M_{cr} and M_{el}^{cr} differ only in the fourth figure after the decimal point, and this difference decreases with increasing relaxation time.

In the domain $M < M_{cr}$, variation of the root s_1 with an increase in M was investigated. For values $M \sim 0.1M_{cr}$, $\mathrm{Re}\, s_1 < \mathrm{Re}\, s_1^{el}$ (the difference is within several percent); at $M > 0.1M_{cr}$, the roots s_1 and s_1^{el} coincide

Table 2

θ	M_{cr}	M_{cr}^{el}
0	0.096066	0.096030
$\frac{3\pi}{8}$	0.253636	0.253543
$\frac{58\pi}{128}$	0.714807	0.714590
$\frac{59\pi}{128}$	1.737786	1.737783
$\frac{62\pi}{128}$	1.727327	1.727324
$\frac{\pi}{2}$	1.725347	1.725344

with an accuracy to the fourth decimal place. This is also a new mechanical effect.

FLOW AROUND A STRIP AT AN ARBITRARY ANGLE

We take the solution to Eq. (3) in the form of a trinomial Bubnov–Galerkin approximation:

$$w = (c_k(t)\sin k\pi y)\exp(-i\alpha x), \quad k = 1, 2, 3.$$

Using the well-known procedure associated with Laplace images, we arrive at the following set of linear equations with respect to $c_k(s)$:

$$\begin{aligned}
&(\lambda_1\mu_1 + B_2)\cdot c_1(s) - \frac{8}{3}a_3 M\sin\theta\cdot c_2(s) = Q_1(s),\\
&\frac{8}{3}a_3 M\sin\theta\cdot c_1(s) + (\lambda_1\mu_2 + B_2)c_2(s)\\
&\quad - \frac{24}{5}a_3 M\sin\theta\cdot c_3(s) = Q_2(s),\\
&\frac{24}{5}a_3 M\sin\theta\cdot c_2(s) + (\lambda_1\mu_3 + B_2)\cdot c_3(s) = Q_3;
\end{aligned} \tag{6}$$

where $\lambda_1 = 1 - \frac{\lambda}{s+1}$, $B_2 = s(a_1 s + a_2) - i\alpha M a_3\cos\theta$, and $\mu_k = (a^2 + k^2\pi^2)^2$. The polynomials $Q_k(s)$ are determined from the initial data.

The behavior of solutions $c_k(t)$ to set (6) is characterized by the roots of its determinant (a polynomial of the ninth power); as previously, we have found the root s_1 that most rapidly approaches the imaginary axis with an increase in M. We have also found the critical flutter velocity: $M_{cr} = \min_{\alpha} M^*(\alpha)$ provided that $P_9(iy) = 0$ and $iy = s_1^*$. The calculation results are presented in Table 2 (the values of the parameters are the same: $\beta = 0.1$ and $\lambda = 0.1$).

The principal conclusion remains the same: the critical flutter velocity M_{cr} coincides with M_{cr}^{el}. The second important result consists in the fact that, in the vicinity of angle $\theta = \frac{\pi}{2}$ (similarly to the elastic problem), there exists an angle θ_0 near which (on the left) M_{cr} sharply increases, i.e., the plot of $M_{cr}(\theta)$ has a vertical tangent line. The character of strip vibrations drastically changes after the angle θ has passed through θ_0.

REFERENCES

1. G. S. Larionov, in *Problems of Computational and Applied Mathematics* (Tashkent, 1970), No. 3, p. 156 [in Russian].
2. V. I. Matyash, Mekh. Polimerov, No. 6, 1077 (1971).
3. G. S. Larionov, Izv. Akad. Nauk SSSR, Mekh. Tverd. Tela, No. 4, 95 (1974).
4. A. A. Il'yushin, G. S. Larionov, and A. N. Filatov, Dokl. Akad. Nauk SSSR **188**, 49 (1969) [Sov. Phys. Dokl. **14**, 931 (1969)].
5. I. A. Kiĭko, Prikl. Mat. Mekh. **60** (1), 172 (1996).

Translated by Yu. Vishnyakov

Doklady Physics, Vol. 50, No. 3, 2005, pp. 161–164. Translated from Doklady Akademii Nauk, Vol. 401, No. 3, 2005, pp. 345–348.

MECHANICS

Problem of Designing an Aerodynamic Profile with Assigned Characteristics of Electromagnetic Scattering

M. S. Soppa

Presented by V.N. Monakhov October 4, 2004

Received October 22, 2004

INTRODUCTION

In this paper, we propose a combined solution to the problem of determining the shape of a profile that possesses the property of streamline flow around its leading edge and an electromagnetic-scattering level close to the assigned value. These tasks cannot be solved separately because they are connected with each other by the unknown shape of the profile surface.

Thus, we consider the scattering of a plane monochromatic *E*- or *H*-polarized electromagnetic wave on an aerodynamic profile with the perfectly conducting surface *S*. In an exterior domain D_S, for the nonzero field component (this is either $u = E_z(x, y)$ or $u = H_z(x, y)$ in the case of *E*- or *H*-polarization, respectively), the Helmholtz equation

$$\frac{\partial^2 u}{\partial x^2} + \frac{\partial^2 u}{\partial y^2} + k^2 u = 0, \quad (x, y) \in D_S \tag{1}$$

is valid with its boundary conditions

$$u(x, y) - \frac{W}{ikW_0}\frac{\partial u_0(x, y)}{\partial n} = 0, \quad (x, y) \in S, \tag{2}$$

or

$$\frac{\partial u(x, y)}{\partial n} - ik\frac{W}{W_0}u_0(x, y) = 0, \quad (x, y) \in S \tag{3}$$

in the case of *E*- or *H*-polarization, respectively. Here, *W* is the surface impedance, i.e., the complex-valued function of the arc coordinate of the boundary contour. This function describes processes occurring in the conductor surface layer that interacts with the electromagnetic field; $k = \frac{2\pi}{\lambda}$; λ is the wavelength; $W_0 = 120\pi = \sqrt{\frac{\mu}{\varepsilon}}$ is the wave resistance of the free space; the symbol $\frac{\partial}{\partial n}$ denotes differentiation over the outer normal; and u_0 is the solution to the direct problem in the case of a perfectly conducting surface ($W = 0$). For the reflected field at infinity, the asymptotic condition for radiation must be valid.

An incompressible potential flow around a profile is described by the Laplace equation for the velocity potential:

$$\frac{\partial^2 \Phi}{\partial x^2} + \frac{\partial^2 \Phi}{\partial y^2} = 0, \quad (x, y) \in D_S, \tag{4}$$

with the impermeability boundary condition:

$$\frac{\partial \Phi}{\partial n} = 0, \quad (x, y) \in S. \tag{5}$$

At the profile trailing edge, the Joukowski–Chaplygin condition is posed that expresses the finiteness of the velocity at the flow trailing point.

The inverse problem for the reconstruction of the unknown profile-surface segment $S_0 \subseteq S$ is considered in the following formulation. It is necessary to find a set of values r_i, $i = 1, 2, \ldots, L$, which parametrically determine the desired surface segment S_0 and provide:

(i) approximation (at a reasonable level of accuracy) to the prescribed scattering diagram;

(ii) shock-free incoming flow around the profile (streamline flow around the profile leading edge).

We now assume that the scattering diagram is given by its complex values at a finite number of far-field points: $e_a(\varphi)$, $\varphi \in \{\varphi_j, j = 1, 2, \ldots, m\}$; φ is the polar angle; $2m = L - 1$ [for *H*-polarization, the function $h_a(\varphi)$ is given]. The criterion of the approximation to the given scattering diagram (in the mean-square sense) is

$$J_1 \equiv \sum_{j=1}^{m} |e(\varphi_j) - e_a(\varphi_j)|^2 \to \min. \tag{6}$$

The shock-free behavior at the input, as a component of the adaptive-wing concept, corresponds to a load on the profile leading edge, which is close to zero.

Novosibirsk State University of Architecture and Building (Sibstrin), Novosibirsk, 630000 Russia
e-mail: soppa@ngs.ru

1028-3358/05/5003-0161$26.00

In the case of a thin profile, this provides a considerable decrease in the drag and an increase in the aerodynamic efficiency. Assuming the profile to be thin and its centerline to be slightly bent, we consider that boundary condition (5) is valid for the profile basis surface (chord). Then, the shock-free condition in terms of pressure factor takes the form $C_p(0) = 0$. When we apply the panel method to model flows around a profile, it is necessary that the vortex-layer density at the chord forepart be zero. We represent the variational analog of this equality as

$$J_2 \equiv |\gamma(0)| \to \min. \tag{7}$$

This condition arising from aerodynamic concepts complements the insufficiently determinate ($2m < L$) electrodynamic problem of identifying the profile shape.

It should be noted that in this situation, various additional conditions, for example, of an isoparametric type, may be given. In particular, if we need to maintain a constant lifting force, e.g., using the corresponding deflection of flaps, then we obtain the relationship

$$C_{y_a} = C^0_{y_a}. \tag{8}$$

A METHOD FOR A COMBINED SOLUTION TO THE PROBLEM

The problems formulated above are both aerodynamic and electrodynamic. They cannot be solved separately because their solutions are connected with each other by the unknown profile-contour segment S_0. We assume that the desired parameters $\{r_i\}$ are moduli of radii vectors of the segment S_0 in support cross sections with polar angles ψ_i, $i = 1, 2, \ldots, L$.

In order to numerically solve the electrodynamic part of the problem, we employ the method described in [1]. This method makes it possible to skip to the integro-operator equation. This equation is nonlinear because the integration domain $S(r(\psi))$ includes the segment S_0 to be determined, namely,

$$\frac{q}{2\pi k W_0}\int\limits_{S(r(\psi))}\left(gD^{-1}C + i\frac{\partial g}{\partial n}\right)W\frac{\partial u_0}{\partial n}dS_P = e_a(M) \tag{9}$$
$$-\frac{q}{2\pi}\int\limits_{S(r(\psi))}\frac{\partial u_0}{\partial n}g\,dS_P, \quad P \in S(r(\psi)), \quad M \in S_R,$$

and

$$\frac{kq}{2\pi W_0}\int\limits_{S(r(\psi))}\left(ig - \frac{\partial g}{\partial n_P}C^{-1}D\right)u_0 W dS_P \tag{10}$$
$$= h_a(M) + \frac{q}{2\pi}\int\limits_{S(r(\psi))}\frac{\partial g}{\partial n_P}u_0 dS_P, \; P \in S(r(\psi)), \; M \in S_R,$$

for the *E*- and *H*-polarization, respectively. Here, S_R is the circular contour of radius R (R is sufficiently large); $q = \sqrt{R}\,e^{-ikR}$; $g(M, P)$ is the fundamental solution to the Helmholtz equation; C and D are the operators inherent in the direct problem for a perfectly conducting surface S in the case of the *H*- and *E*-polarization, respectively. Thus, we have applied the method of artificial immersion in the more general problem, for which surface impedance W is considered to be unknown in the desired profile segment.

The aerodynamic problem is solved by the panel method described in [2] with the boundary conditions transferred to the basis plane. Reversing the aerodynamic-influence matrix A, we express the vortex-layer intensity γ in terms of local angles of attack δ of panels. As a result, condition (7) can be rewritten in the form

$$\gamma_1 = \sum_{p=1}^{NW}(A^{-1})_{p,1}(\delta_p - \alpha_0 + \delta^0_p) = 0, \tag{11}$$

where α_0 is the angle of attack, δ^0_p are angles of the panel deflection caused by the initial deformation of the profile centerline, δ_p are varied deflection angles, and NW is the number of panels in which the profile chord is partitioned.

If the value of the lifting force is fixed, then the condition of inverse problem (8) results in the appearance of the additional relationship

$$2\sum_{p=1}^{NW}\bar{s}_p\bar{\gamma}_p = C^0_{y_a},$$

where $\bar{s}_p$ is the dimensionless panel length, and $\bar{\gamma}_p$ is the value of vortex-layer intensity at the panel center. In this case, the flap deflection angle δ_f is added to the number of desired variables.

In [3], an efficient method was indicated for reconstructing the surface impedance, which uses the given field in the case of fixed geometry. This method makes it possible to determine the operator $\mathbf{G}$ upon solving Eqs. (9) or (10):

$$\mathbf{W} = \mathbf{G}(\mathbf{r}).$$

Here and below, the vector quantities are discrete analogs of the corresponding continuous functions.

Relationship (11) allows us to express the load on the profile leading edge in terms of the variable $\mathbf{r}$:

$$\gamma_1 = \mathbf{Y}(\mathbf{r}).$$

Introducing the notation $\mathbf{Z} = \{\mathbf{G}, \mathbf{Y}\}$, $\mathbf{X} = \{\mathbf{W}, \gamma_1\}$, we can write out the equality

$$\mathbf{X} = \mathbf{Z}(\mathbf{r}).$$

It is worth noting at this point that the desired solution to the inverse problem corresponds to the zero values of the parameters $\mathbf{W}$ and γ_1. Therefore, instead of

the totality of extremal problems (6) and (7), we arrive at the nonlinear operator equation

$$\mathbf{Z}(\mathbf{r}) = 0. \quad (12)$$

Solving this equation by Newton's method, we obtain the shape of the profile leading edge that exhibits streamline flow around the front edge in the cruising regime and, furthermore, possesses a scattering diagram close to the assigned one.

CONVERGENCE OF THE NUMERICAL SOLUTION TO THE OPERATOR EQUATION

Regularization of the auxiliary discrete problem under conditions of a fixed geometry, which is based on the Tikhonov zeroth-order regularizer [4], allows us to calculate $\mathbf{W}$ and γ_1 with the estimate of the norm, which depends on the regularization parameter α:

$$\|\mathbf{X}\| \le \varepsilon_1(\alpha, \|\Delta\mathbf{r}\|), \quad (13)$$

where $\Delta\mathbf{r}$ is the increment of the vector $\mathbf{r}$ that determines the shape of the segment S_0. Upon solving nonlinear operator equation (12) by Newton's method and after discretization, we can calculate the matrix of finite-difference derivatives

$$\mathbf{DZ} = \left(\frac{\partial \mathbf{Z}_i}{\partial r_j}\right), \quad i, j = 1, 2, \ldots, L.$$

The next approximation $\mathbf{r}_k$ is found from the formula

$$\mathbf{r}_k = \mathbf{r}_{k-1} - \mathbf{DZ}^{-1}\mathbf{X}_{k-1}, \quad k = 1, 2, \ldots. \quad (14)$$

In this case,

$$\mathbf{X}_{k-1} = \mathbf{Z}(\mathbf{r}_{k-1}). \quad (15)$$

We now study the convergence of the vector $\mathbf{X}_k$ to zero. The Taylor expansion of relationship (15) in the vicinity of $\mathbf{r}_{k-2}$ allows us to find the estimate

$$\|\mathbf{X}_{k-1}\| \le \frac{1}{2}\|\partial^2\mathbf{Z}(\boldsymbol{\xi})\|\|\mathbf{DZ}^{-1}\|^2\|\mathbf{X}_{k-2}\|^2.$$

The right-hand side of this equality contains the norm for the second-derivative matrix as well as the norm for the inverse first-derivative matrix. We denote

$$D_2 = \max\|\partial^2\mathbf{Z}(\xi)\|, \quad D_1 = \max\|\mathbf{DZ}^{-1}\|.$$

Relationship (13) ensures the choice of initial parameters such that $\|\mathbf{X}_0\| \le \dfrac{1}{D_1^2 D_2}$. Then,

$$\|\mathbf{X}_k\| \le \left(\frac{1}{2}\right)^{1+2+4+8+\ldots+2^{k-1}}\|\mathbf{X}_0\| \le \left(\frac{1}{2}\right)^{2^k-1}\|\mathbf{X}_0\|.$$

Thus, assuming the smoothness and boundedness of the matrix norms $\partial^2\mathbf{Z}$ and $\mathbf{DZ}^{-1}$, the initial approximation taken in sufficiently close vicinity to the exact solution guarantees convergence of the vector $\mathbf{X}_k$ to zero at a velocity higher than that of a geometric progression. Analogous estimates and conclusions are also valid for the sequence $\{\Delta\mathbf{r}_k\}$. By virtue of this fact, the sequence

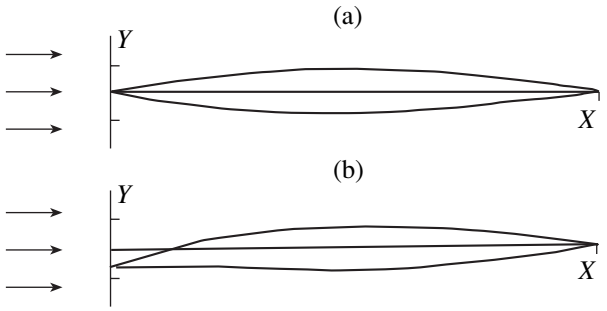

Fig. 1. Contours for (a) the initial profile and (b) the profile obtained as a result of solving the inverse problem.

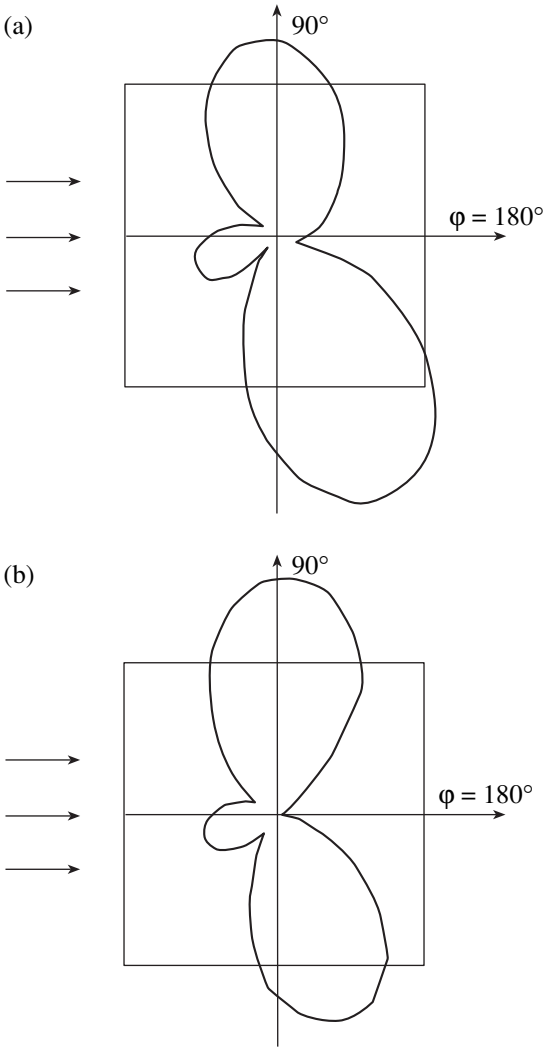

Fig. 2. Scattering diagram for (a) the initial profile and (b) the profile obtained as a result of solving the inverse problem.

of vectors $\{\mathbf{r}_k\}$ converges at the same velocity to the solution of Eq. (12).

THE RESULTS OF THE NUMERICAL EXPERIMENT

We analyzed as an example the problem of reconstructing the shape of the leading edge of an aerodynamic profile when the shock-free behavior (streamline flow around the profile) had been combined with the assigned level of electromagnetic reflection in fixed directions. In addressing this problem, the most convenient approach involves parameterization of the profile contour not by the polar angle ψ, but by another method traditional in aerodynamics. We allude to the use of equations $y_u(x)$ and $y_l(x)$ for the upper and lower profile surfaces, respectively, where x is the dimensionless coordinate along the profile chord.

The initial (undeformed) profile was taken symmetric and lens-shaped. The wavelength λ is linked with the chord length b by the relation $\frac{\lambda}{b} = 1.23$. Figure 1a shows the shape of the initial contour. Variation of the parameters was performed by flanging the profile leading edge in the segment $0 \le x \le 0.2$, having taken into account the correlation relationship $y_u(0) = y_l(0)$. The cruiser regime of flow around the profile was assigned at the angle of attack $\alpha_0 = 3°$. The level of electromagnetic reflection was set in the form of complex values of the magnetic field in the measurement directions $\varphi \in [-25°; 25°]$, irradiation being performed from the leading-edge side at the incidence angle $\varphi = 0$ of a plane H polarized wave.

As a result of solving the inverse problem, the desired profile contour was obtained (Fig. 1b). In Fig. 2, scattering diagrams are presented for the bistatic location of the initial and resulting forms of the adaptive profile. The scattering diagram is asymmetric with respect to the horizontal axis due to the nonzero angle of attack α_0.

Analysis of the plots shows that flanging the leading edge results in the redistribution of reflection intensity in favor of the upper hemisphere.

REFERENCES

1. M. S. Soppa, Izv. Vyssh. Uchebn. Zaved., Radiofiz. **42**, 452 (1999).
2. V. V. Kraus, *Panel Methods in Aerodynamics. Numerical Methods in Fluid Dynamics* (Mir, Moscow, 1981) [in Russian].
3. M. S. Soppa and E. E. Ershova, Avtometriya, No. 2, 56 (1997).
4. A. N. Tikhonov and V. Ya. Arsenin, *Methods of Solving Ill-Posed Problems* (Nauka, Moscow, 1986; Halsted Press, New York, 1977).

Translated by G. Merzon